

Material Matters™

Volume 11, Number 4

ALDRICH
Materials Science

Advances in Magnetic Materials

Bringing Technology Together

RECENT PROGRESS IN
SPINTRONIC MATERIALS

SOFT MAGNETIC NANOCRYSTALLINE ALLOYS:
MATERIALS AND MODELS

ADDITIVE MANUFACTURING
OF PERMANENT MAGNETS

RESPONSIVE RARE-EARTH MATERIALS
AND THEIR APPLICATIONS



Introduction

Welcome to the fourth issue of *Material Matters*[™] for 2016. Magnetic materials have become the backbone of recent technological advancements with applications spanning modern electronics to alternative energy harvesting. By allowing for both rapid information encoding and static, long-term information storage, magnetic spin forms the basis for energy efficient, high-capacity information storage devices. Still other unique magnetostructural and stimuli-responsive properties of magnetic materials make them useful for other applications such as refrigeration, actuation and even energy harvesting. A number of important classes of magnetic materials and their applications are discussed in this issue of *Material Matters*[™].

In our first article, Professor Arunava Gupta (University of Alabama, USA) discusses recent developments in spintronics. Here the authors review the spintronic properties of a number of Heusler alloys, magnetic oxides and multiferroics and offer a future perspective on the potential impact of these materials.

Professor Victorino Franco (University of Seville, Spain) discusses soft magnetic nanocrystalline materials in the second article. Here the characteristic magnetic properties of an important class of nanocrystalline soft magnets, such as FINEMET[®], NANOPERM[®], HITPERM, and NANOMET[®], along with their dependence on composition and processing conditions are reviewed.

In the third article, Professor M.P. Paranthaman (Oak Ridge National Laboratory, USA) reviews the properties of permanent magnets. The role of additive manufacturing in minimizing waste of the rare earth elements during the manufacturing of permanent magnets is also presented.

Finally, in the fourth article, Dr. Yaroslav Mudryk (Ames Laboratory, USA) presents an overview of multifunctional responsive rare-earth based materials. The magnetostructural properties of several $R_5(\text{Si,Ge})_4$ (R = rare-earth element) and RM_2 [M = either *p*- (e.g., Mg, Al) or *d*- (e.g., Fe, Ni, Co) metal] compounds and their unusual responsiveness to external stimuli is discussed in detail.

Each of these articles is accompanied by a list of relevant materials available from Sigma-Aldrich[®] Materials Science. For additional product information, visit sigma-aldrich.com/matsci. Please send your comments or suggestions for *Material Matters*[™] or your product suggestions to matsci@sial.com.

About Our Cover

Novel magnetic materials are driving advances in magnetic storage, refrigeration, sensing and mobility. Cellular phones, tablets, laptops, televisions, cars, and airplanes are all essential devices for modern daily life and magnetic materials are critical components for each of them. In this issue, the foreground cover art highlights some of these everyday items on a colorful representation of a magnetic field.



Niraj Singh, Ph.D.
Aldrich Materials Science

Material Matters[™]

Vol. 11, No. 4

Aldrich Materials Science
Sigma-Aldrich Co. LLC
6000 N. Teutonia Ave.
Milwaukee, WI 53209, USA

To Place Orders

Telephone 800-325-3010 (USA)
FAX 800-325-5052 (USA)

International customers, contact your local Sigma-Aldrich office (sigma-aldrich.com/worldwide-offices).

Customer & Technical Services

Customer Inquiries 800-325-3010
Technical Service 800-325-5832
SAFC[®] 800-244-1173
Custom Synthesis 800-244-1173
Flavors & Fragrances 800-227-4563
International 314-771-5765
24-Hour Emergency 314-776-6555
Safety Information sigma-aldrich.com/safetycenter
Website sigma-aldrich.com
Email aldrich@sial.com

Subscriptions

Request your **FREE** subscription to *Material Matters*:

Phone 800-325-3010 (USA)
Mail Attn: Marketing Communications
Aldrich Chemical Co., Inc
Sigma-Aldrich Co. LLC
P.O. Box 2060
Milwaukee, WI 53201-2060
Website aldrich.com/mm
Email sams-usa@sial.com

Online Versions

Explore previous editions
of *Material Matters* aldrich.com/materialmatters

Material Matters (ISSN 1933-9631) is a publication of Aldrich Chemical Co. LLC. Aldrich is a member of the Sigma-Aldrich Group.

©2016 Sigma-Aldrich Co. LLC. All rights reserved. SIGMA, SAFC, SIGMA-ALDRICH, ALDRICH and SUPELCO are trademarks of Sigma-Aldrich Co. LLC, registered in the US and other countries. Material Matters is a trademark of Sigma-Aldrich Co. LLC. 3DXMax, 3DXNano, 3DXTech, and iOn are trademarks of 3DXTech. FINEMET is a registered trademark of Hitachi Metals, Ltd. NANOMET is a trademark of TOHOKU MAGNET INSTITUTE CO., LTD. NANOPERM is a trademark of MAGNETEC GmbH. *ReagentPlus* is a registered trademark of Sigma-Aldrich Co. LLC. Sigma-Aldrich, Sigma, Aldrich, Supelco, and SAFC brand products are sold by affiliated Sigma-Aldrich distributors. Purchaser must determine the suitability of the product(s) for their particular use. Additional terms and conditions may apply. Please see product information on the Sigma-Aldrich website at www.sigmaaldrich.com and/or on the reverse side of the invoice or packing slip. Sigma-Aldrich Corp. is a subsidiary of Merck KGaA, Darmstadt, Germany.

Table of Contents

Articles

Recent Progress In Spintronic Materials	97
Soft Magnetic Nanocrystalline Alloys: Materials and Models	104
Additive Manufacturing of Permanent Magnets	111
Responsive Rare-Earth Materials and Their Applications	120

Featured Products

Substrates for Thin Film Deposition	101
A list of substrates for deposition	
Sputtering Targets	101
A list of high-purity sputtering targets	
Vapor Deposition Precursors for Magnetic Thin Film Formation	101
A selection of transition metal vapor deposition precursors	
Magnetic Materials	109
A selection of magnetic oxides, alloys, and nanomaterials	
Metallic Powders	116
A selection of metal powders for magnetic applications	
3D Printable Graphene Ink	117
A list of graphene inks for 3D printing	
3D Printing Filaments	118
An assortment of 3D printing filaments	
Metallic Precursors for Magnetic Alloys	124
A selection of various metals	
Magnetocaloric Materials	126
Materials shown to exhibit a magnetocaloric effect	

Your Materials Matter



Bryce P. Nelson

Bryce P. Nelson, Ph.D.
Materials Science Initiative Lead

We welcome fresh product ideas. Do you have a material or compound you wish to see featured in our Materials Science line? If it is needed to accelerate your research, it matters. Send your suggestion to matsci@sial.com for consideration.

Prof. Robert Hamers of the University of Wisconsin – Madison (USA) recommended the addition of fluorescent nanodiamonds (Prod. No. **900173**) containing Nitrogen-Vacancy (NV) centers to our catalog. NV-containing nanodiamonds are fluorophores that provide infinite photostability, a large Stokes shift, high biocompatibility, and versatile surface functionalization.¹ High photostability is essential for applications requiring extended or powerful illumination, from tracking particles through cell lines to super-resolution techniques.² Unlike many fluorescent nanoparticles, these unique materials also exhibit low cytotoxicity since their fluorescence does not rely on heavy metals. Moreover, the nature of a nanodiamond sp³ hybridized carbon surface allows for a variety of robust surface modifications that enable straightforward bioconjugation.

Microscopy applications include confocal and high resolution fluorescent bioimaging, cathodoluminescent imaging, and stimulated emission depletion (STED) imaging, among others.³⁻⁵ NV centers are also spin active, allowing sensitivity to local magnetic and electric fields. As such, they have the potential to be used as sensors in optically detected magnetic resonance and nanothermometry and for the detection of local molecular concentrations.⁶

References

- (1) Krueger, A.; Lang, D. *Adv. Funct. Mater.* **2012**, *22*, 890.
- (2) Hsiao, W. W.; et al. *Acc. Chem. Res.* **2016**, *49*, 400.
- (3) Hens, S. C.; et al. *Diamond Relat. Mater.* **2008**, *17*, 1858.
- (4) Hui, Y.; et al. *Optics Express* **2010**, *18*, 5896.
- (5) Vijayanthimala, V.; et al. *Expert Opin. Drug Del.* **2014**, *12*, 1.
- (6) Schirhagl, R.; et al. *Annu. Rev. Phys. Chem.* **2014**, *65*, 83.

Fluorescent nanodiamond

Nanodiamond
70 nm
>60 Nitrogen vacancy per particle
1 mg/mL H₂O

900173-5ML

5 mL

ULTRA-HIGH PURITY MATERIALS

We are pleased to offer a large selection of ultra-high purity metals, salts and oxides with purity of 99.999% or higher.

Our portfolio offers over 300 metals, salts, and oxides with high trace metal purities and applications in areas including:

- Photovoltaics
- Magnetic Memory
- Phosphor Materials
- Biomedical Applications
- Nanoparticle Synthesis
- Electronic Devices

Product Description	Prod. No.
Metals	
Tellurium, pieces, 99.999% trace metals basis	204544
Aluminum, wire, diam. 1.0 mm, 99.999% trace metals basis	266558
Gold, beads, 1-6 mm, 99.999% trace metals basis	326542
Copper, powder, 99.999% trace metals basis	203122
Zinc, foil, thickness 0.25 mm, 99.999% trace metals basis	267619
Indium, beads, diam. 2-5 mm, 99.999% trace metals basis	264113
Bismuth, pieces, 1-12 mm, 99.999% trace metals basis	556130
Copper, foil, thickness 1.0 mm, 99.999% trace metals basis	266744
Mercury, electronic grade, 99.9999% trace metals basis	294594
Germanium, chips, 99.999% trace metals basis	203343
Oxides	
Lead(II) oxide, 99.999% trace metals basis	203610
Antimony(III) oxide, 99.999% trace metals basis	202649
Iron(III) oxide, $\geq 99.995\%$ trace metals basis	529311
Bismuth(III) oxide, powder, 99.999% trace metals basis	202827
Zinc oxide, 99.999% trace metals basis	204951
Germanium(IV) oxide, powder, 99.999% trace metals basis	483001
Holmium(III) oxide, powder, 99.999% trace metals basis	229679
Copper(II) oxide, 99.999% trace metals basis	203130
Selenium dioxide, 99.999% trace metals basis	204315
Nickel(II) oxide, $\geq 99.995\%$ (Trace Metals Analysis)	481793

Product Description	Prod. No.
Salts	
Gold(III) chloride hydrate, 99.999% trace metals basis	254169
Ammonium acetate, 99.999% trace metals basis	372331
Aluminum chloride, anhydrous, powder, 99.999% trace metals basis	563919
Lead(II) iodide, 99.999% trace metals basis	203602
Zinc chloride, 99.999% trace metals basis	229997
Silver nitrate, 99.9999% trace metals basis	204390
Copper(I) iodide, 99.999% trace metals basis	215554
Nickel(II) nitrate hexahydrate, 99.999% trace metals basis	203874
Copper(I) bromide, 99.999% trace metals basis	254185
Sodium carbonate, anhydrous, powder, 99.999% trace metals basis	451614
Gallium(III) chloride, beads, anhydrous, $\geq 99.999\%$ trace metals basis	427128
Indium(III) chloride, 99.999% trace metals basis	203440
Ammonium sulfate, 99.999% trace metals basis	204501
Cesium chloride, $\geq 99.999\%$ trace metals basis	203025
Cobalt(II) nitrate hexahydrate, 99.999% trace metals basis	203106
Lanthanum(III) chloride heptahydrate, 99.999% trace metals basis	203521



For a complete list of ultra-high purity products, visit aldrich.com/uhp

RECENT PROGRESS IN SPINTRONIC MATERIALS



Soubantika Palchoudhury,¹ Karthik Ramasamy,^{2*} Arunava Gupta^{3*}

¹Civil and Chemical Engineering, University of Tennessee at Chattanooga, Chattanooga, Tennessee 37403, USA

²Center for Integrated Nanotechnologies, Los Alamos National Laboratory, Albuquerque, New Mexico 87185, USA

³Center for Materials for Information Technology, The University of Alabama, Tuscaloosa, Alabama 35487, USA

*Email: kramasamy@lanl.gov, agupta@mint.ua.edu

Introduction

Spin-based electronic (spintronic) devices offer significant improvement to the limits of conventional charge-based memory and logic devices which suffer from high power usage, leakage current, performance saturation, and device complexity.^{1,2} Spintronics, as first recognized by Mott in 1936, is the interlinking between the spin and charge degrees of freedom of a material.³ In particular, magnetic materials are highly promising for use in spintronic devices because their electron spin orientation can be readily manipulated through external magnetic fields. The difference in mobility and the population of spin up and spin down electrons in magnetic materials induce a net flow of spin-polarized current. Due to the intrinsic hysteresis properties of ferromagnetic materials, a spintronic device can ideally “remember” the set state for an indefinite time. Consequently, these non-volatile spin-based materials allow significant increase in device density and energy savings while also offering new functionalities.⁴

Current spintronic applications focus primarily on magnetic storage and sensing, using giant magnetoresistance (GMR) and tunneling magnetoresistance (TMR) effects (Figure 1). GMR is observed in thin films with alternate ferromagnetic and non-magnetic metallic spacer layers. The enhanced resistance observed when ferromagnetic layers are magnetically aligned anti-parallel to each other, rather than aligned parallel, forms the basis of GMR. A TMR device, in its simplest form, consists of two ferromagnetic metallic electrodes on either side of a very thin non-magnetic insulator layer. Electrons are transmitted from one ferromagnetic electrode to the other through quantum mechanical tunneling across the insulating barrier. Similar to GMR, the resulting tunneling conductance depends on relative alignment of the ferromagnetic layers and is the underlying principle behind TMR. The GMR and TMR effects have been exploited and widely used in hard-drive read heads and, more recently, in magnetic random-access memory (MRAM) devices.

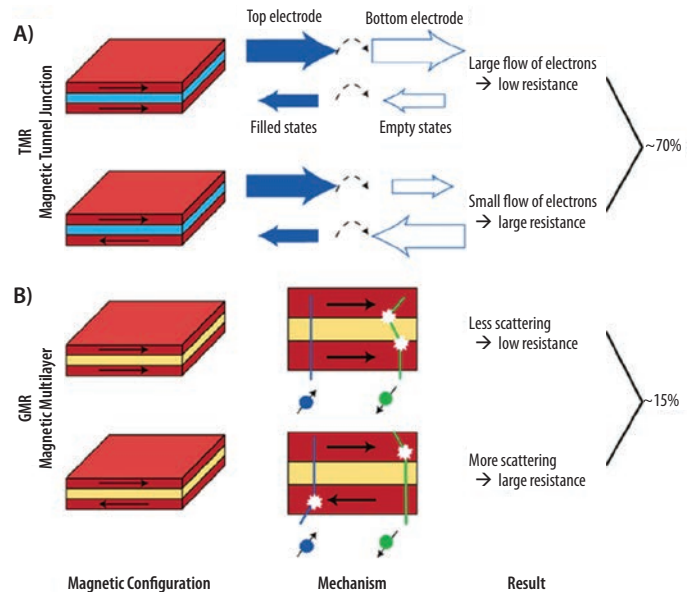


Figure 1. Spintronic devices. A) TMR and B) GMR. Copyright: Nature Materials¹

The control of magnetism and spin has far-reaching potential outside its conventional applications. This is confirmed by many rapidly advancing spintronic subtopics such as current-induced torque, spin Hall effect, spin caloritronics, silicon spintronics, and the spintronics of graphene and topological insulators.⁵ Current-induced magnetization dynamics is based on the principle that a change in the direction of the electron spin from interaction with a thin ferromagnetic layer induces in-plane or perpendicular spin-transfer torque on the ferromagnet. This manipulation of magnetization has become a key tool for the exploration of next-generation devices such as logic-based spin-transistors, miniaturized MRAMs, and high-density data storage. The spin Hall effect, originating from the spin-orbit coupling interaction that orients the electrons perpendicular to the current in a spin-dependent way has emerged as a valuable tool to envisage spin-current measurement technology like field-effect transistors (FETs). Spin caloritronics is based on the spin Seebeck effect, but a complete understanding is still lacking. It is a remarkable concept for generating spin current and can potentially be exploited to enhance the efficiency of heat engines. Silicon spintronics is an attempt to revolutionize information technology through the integration of non-volatile ferromagnetic memory and band-gap engineered semiconductor logic computing.⁶ In addition, recent experimental realization of graphene and topological insulator surface states opens new routes for spin generators (topological insulators) and spin conductors (graphene). Graphene and topological insulators both share the linear Dirac spectrum, but represent two polar opposites of paramagnetic conductor spintronics. Topological insulators are also a key component in fault-tolerant quantum computation as they can be integrated with superconductors to generate Majorana fermions.

Magnetic Oxide Materials

Transition metal oxides exhibit a wide range of tunable magnetic and electrical properties that are very attractive for spintronics. For example, the doped perovskite system $\text{La}_{1-x}\text{Sr}_x\text{MnO}_3$ (LSMO, $x=0.3-0.4$) is both metallic and ferromagnetic, with near-unity spin polarization. In combination with the perovskite material SrTiO_3 as a tunnel barrier, LSMO has exhibited a TMR ratio as high as 1,850%.¹³ But such a high TMR value is observable only at low temperatures. In order to achieve high TMR at RT, magnetic double perovskites that have a higher Curie temperature have been explored. In double perovskites, the formula unit is doubled by the presence of two B cations, i.e., $\text{A}_2\text{B}'\text{B}''\text{O}_6$, ideally with a completely ordered occupation of octahedral sites. Bulk studies identified the compounds $\text{Sr}_2\text{FeMoO}_6$ and $\text{Sr}_2\text{CrReO}_6$ as showing magnetic ordering above RT with promising half-metallic characteristics.¹⁴ But high-quality tunnel junctions based on films of these complex oxides have been challenging to fabricate, primarily because of the narrow process window for high-quality film growth and the propensity for B site disorder that degrades the magnetic properties. Another metallic ferromagnetic oxide of interest is CrO_2 which has been widely used in the past as a particulate medium in magnetic tapes. It has a tetragonal rutile structure with a moment of $2.0 \mu_B/\text{f.u.}$ and a Curie temperature of approximately 400 K. CrO_2 has also been experimentally confirmed to be half-metallic.¹⁵ Novel heterostructures of CrO_2 combined with other members of the rutile family, such as TiO_2 , VO_2 , RuO_2 and SnO_2 , are expected to show exciting spintronic properties. For example, band structure calculations suggest that heterostructures of CrO_2 with metallic or semiconducting rutile oxide spacer layers can potentially exhibit very high magnetoresistance. However, there has been limited work reported thus far on CrO_2 -based devices, primarily because of the difficulties related to thin film synthesis of this metastable phase. The surface of CrO_2 tends to readily reduce into the more stable phase Cr_2O_3 , which is antiferromagnetic. Nevertheless, there has been some success in fabricating rutile heterostructures of CrO_2 , and ongoing investigations indicate the possibility of realizing the full potential of this unique material for spintronics. Spinel phase iron oxide (Fe_3O_4), which is the oldest known magnetic material, is another widely investigated material system for the spintronics applications. It has a high Curie temperature of ~ 850 K and is predicted to exhibit high spin polarization ($\sim 80\%$). Over 500% magnetoresistance ratio has been observed for Fe_3O_4 through nano-contact measurements.¹⁶

While ferromagnetic Fe_3O_4 displays hopping conduction resulting in poor metallic behavior at RT, other ferrites of the spinel family, e.g., NiFe_2O_4 and CoFe_2O_4 , are insulating. These ferrites are widely used for high frequency applications, and thin films of these materials have recently attracted interest in spintronics research for spin filtering and spin caloritronics. By using a magnetic insulator as a tunnel barrier, one can ‘filter’ out spins of one orientation and achieve 100% polarization even without half metals. Effective spin filtering has been demonstrated at low temperatures using ferromagnetic semiconducting EuO .¹⁷ More recently, several insulating spinel ferrites have been shown to act as RT spin filters but, thus far, the TMR for these have been quite low. Another rapidly expanding research field of magnetic insulator-based spintronics involves efficient transport of spin current and magnons without any charge transfer.⁵ This requires magnetic materials with very low damping. The insulating ferrimagnet yttrium iron garnet (YIG, $\text{Y}_3\text{Fe}_5\text{O}_{12}$), which is widely used in microwave and magneto-optical applications, is presently the preferred material for most studies of spin transport and dynamics since it exhibits exceptionally low damping even in thin films. Nevertheless, there is a great need for developing new insulating and semiconducting magnetic oxides for efficient spin generation and transport for room temperature device operation.

Multiferroic Spintronic Materials

Multiferroics are materials in which at least two of the ferroelectric, ferro/antiferromagnetic, and ferroelastic phases co-exist. The technological

appeal of multiferroic materials is huge, particularly for designing multifunctional hybrid spintronic devices, as these materials have the potential to control magnetism with electric fields (Figure 3).¹⁸ Hybrid nanoscale devices based on multiferroics are expected to drastically reduce dissipation losses and have a potential market value worth billions of US dollars. Classic multiferroic materials like antiferromagnetic Cr_2O_3 , boracites, rare-earth ferrites, and manganese perovskites have been known since the 1950s, but these materials have Néel or Curie temperatures below RT or are challenging to grow as thin films. These limitations and a lack of knowledge about the guiding mechanisms behind the multiferroic effect brought the field to a stand-still after initially showing significant promise. Only recently, groundbreaking discoveries in the underlying solid-state physics and synthesis of multiferroic materials have restored the tremendous potential of the field. For industrial application of multiferroic-based devices, the coupling of ferroelectric and ferromagnetic orders in multiferroic materials must be achieved at RT. So far, BiFeO_3 is the only single-phase RT multiferroic material that is ferroelectric while displaying antiferromagnetic order. Nevertheless, BiFeO_3 exhibits reasonable magnetoelectric coupling.¹⁹ It is an example of a direct multiferroic material, meaning application of a magnetic or electric field will directly alter the magnetization or electric polarization of the system, as opposed to the indirect effects observed in composite multiferroic materials.

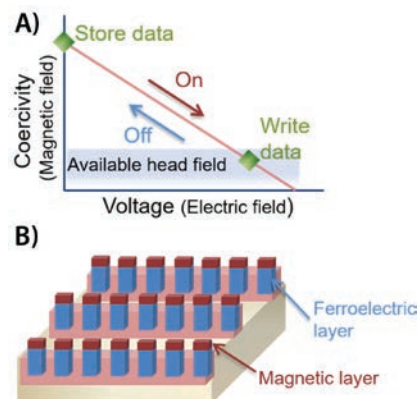


Figure 3. A) Working principle for electrically assisted magnetic recording and B) arrays of magnetic ferroelectric nanoislands with patterned bottom electrodes (pink) for purely electrically driven magnetization reversal in a selected storage unit.

In ABX_3 perovskites like BiFeO_3 , lone electron pairs of the A cation distort the geometry of the BX_3 octahedra. This ‘lone pair’ effect is the key to its multiferroicity. It has been demonstrated that ferroelastic rather than ferroelectric domain switching plays a dominant role in multiferroic BiFeO_3 . But, control of the elastic interactions is a major challenge as it destabilizes the small switched volumes inducing back-switching at zero electric field and loss of non-volatile memory. To eliminate the back-switching, Eom et al. first reported the use of isolated monodomain BiFeO_3 islands. Geometric frustration is another significant mechanism for multiferroics, primarily observed in YMnO_3 .²⁰ Long-range dipole–dipole interactions and rotations of oxygen atoms facilitate a stable ferroelectric state in YMnO_3 . In this hexagonal manganite, the unexpected clamping of ferroelectric domain walls with the magnetic domain walls is driven by a unique lattice distortion, trimerization. Transmission electron microscopy and conductive atomic force microscopy characterization revealed remarkable ‘cloverleaf’ defects where all six structural domains of YMnO_3 merge. The electric polarization changes its sign six times along a loop enclosing these defect sites, creating an elegant demonstration of the geometric frustration mechanism. Another significant mechanism supporting multiferroicity is charge-ordering, particularly found in the RFe_2O_4 family of compounds (R = rare-earth element from Dy to Lu and Y). In LuFe_2O_4 , the crystal structure contains alternate packing of triangular lattices of rare-earth elements, iron, and oxygen. Equal amounts

of Fe^{2+} and Fe^{3+} occupy equivalent sites in the lattice. Consequently, RFe_2O_4 is a charge-frustrated system of triangular lattices because the pairing of opposite charges (Fe^{2+} and Fe^{3+}) based on Coulomb's law causes degeneracy in the lowest energy for charge configuration. These materials facilitate efficient electron transport and, hence, less coupling of polarization switching with lattice distortion. Therefore, the RFe_2O_4 class of multiferroics may be a key milestone to design fatigue-free charge capacitors. Multiferroic manganites, RMnO_3 (R = rare-earth element) and TbMn_2O_4 , on the other hand, exhibit spin-effect based magnetoelectricity. In these materials, magnetic long-range order and the lack of reflection symmetry in the arrangement of magnetic dipoles is responsible for ferroelectricity. The frustrated-spin systems show remarkable magnetocapacitance, opening new routes for spintronic applications.

In summary, multiferroic materials demonstrate a complex interplay between structural, electric, and magnetic properties, which is a key milestone toward multifunctional spintronic devices. Several promising multiferroic materials like Y-type hexaferrite [or $(\text{Ba}, \text{Sr})_2\text{Zn}_2\text{Fe}_{12}\text{O}_{22}$, $\text{Ba}_2\text{Mg}_2\text{Fe}_{12}\text{O}_{22}$], Z-type hexaferrites (or $\text{Sr}_3\text{Co}_2\text{Fe}_{24}\text{O}_{41}$ and CuO), GdFeO_3 , CdCr_2S_4 , and indium perovskites have been reported thus far. However, RT multiferroicity in single-phase materials has been challenging to achieve. The general focus in the field is shifting toward advanced characterization techniques, better thin-film fabrication tools, device architecture, and understanding of the domain-interface effects.

Perspective

Spintronics has far-reaching potential in both memory and logic computing devices because it exploits the phenomena that interlink the spin and charge degrees of freedom. Currently half-metallicity at RT and realizing perpendicular anisotropy in nanoscale devices at RT are the two key targets for the synthesis of new spintronic materials.²¹ With breakthroughs in the fundamental understanding of solid-state physics and fast-paced advancements in material development, these goals are soon to be met, as summarized in this review. Based on the current state of the research, we can anticipate all-Heusler and all-oxide junctions to be implemented in MRAM and high-frequency devices in the foreseeable future (Figure 4).

Acknowledgments

This work was supported by NSF Grant no. ECCS-1509875. We gratefully acknowledge UA-MINT Center and Center for Integrated Nanotechnologies, Los Alamos National Laboratory for additional support. SP thanks CECS, UT Chattanooga for support.

References

- (1) Moodera, J. S.; LeClair, P. *Nat. Mater.* **2003**, *2*, 707.
- (2) Bao, N.; Gupta, A., *Inorganic Spintronic Materials*. In *Encyclopedia of Inorganic and Bioinorganic Chemistry*, John Wiley & Sons, L., Ed. **2013**; pp 1–15.
- (3) Hirohata, A.; Sukegawa, H.; Yanagihara, H.; Zutic, I.; Seki, T.; Mizukami, S.; Swaminathan, R. *IEEE Trans. Mag.* **2015**, *51*, 1.
- (4) Scheunert, G.; Heinonen, O.; Hardeman, R.; Lapicki, A.; Gubbins, M.; Bowman, R. M. *Appl. Phys. Rev.* **2016**, *3*, 011301.
- (5) Sinova, J.; Zutic, I. *Nat. Mater.* **2012**, *11*, 368.
- (6) Jansen, R. *Nat. Mater.* **2012**, *11*, 400.
- (7) Han, W. *APL Mater.* **2016**, *4*, 032401.
- (8) Graf, T.; Felser, C.; and Parkin, S. P. *Prog. Solid State Chem.* **2011**, *39*, 1.
- (9) Kim, J.-H.; Lee, J.-B.; An, G.-G.; Yang, S.-M.; Chung, W.-S.; Park, H.-S.; Hong, J.-P. *Sci. Rep.* **2015**, *5*, 16903.
- (10) Nayak, A. K.; Nicklas, M.; Chadov, S.; Shekhar, C.; Skourski, Y.; Winterlik, J.; Felser, C. *Phys. Rev. Lett.* **2013**, *110*, 127204.
- (11) Wadley, P.; Novák, V.; Campion, R. P.; Rinaldi, C.; Martí, X.; Reichlová, H.; Železný, J.; Gazquez, J.; Roldan, M. A.; Varela, M.; Khalyavin, D.; Langridge, S.; Kriegner, D.; Mácá, F.; Mašek, J.; Bertacco, R.; Holý, V.; Rushforth, A. W.; Edmonds, K. W.; Gallagher, B. L.; Foxon, C. T.; Wunderlich, J.; Jungwirth, T. *Nat. Commun.* **2013**, *4*, 2322.
- (12) Wang, C.; Meyer, J.; Teichert, N.; Auge, A.; Rausch, E.; Balke, B.; Hutten, A.; Fecher, G.-H.; Felser, C. *J. Vac. Sci. Technol. B* **2014**, *32*, 020802.
- (13) Bowen, M.; Bibes, M.; Barthélémy, A.; Contour, J.-P.; Anane, A.; Lemaître, Y.; Fert, A. *Appl. Phys. Lett.* **2003**, *82*, 233.
- (14) Serrate, D.; Teresa, J. M. D.; Ibarra, and M. R. J. *Phys.: Condens. Matter.* **2007**, *19*, 23301.
- (15) Ji, Y.; Strijkers, G. J.; Yang, F. Y.; Chien, C. L.; Byers, J.M.; Anguelouch, A.; Xiao, G.; Gupta, A. *Phys. Rev. Lett.* **2001**, *86*, 5585.
- (16) Yanase, A.; Siratori, K.; *J. Phys. Soc. Jpn.* **1984**, *53*, 312.
- (17) Moodera, J.; Santos, T. S.; Nagahama, T.; *J. Phys.: Condens. Matter.* **2007**, *19*, 165202.
- (18) Hu, J.-M.; Chen, L.-Q.; Nan, C.-W. *Adv. Mater.* **2015**, *28*, 15.
- (19) Heron, J. T.; Bosse, J. L.; He, Q.; Gao, Y.; Trassin, M.; Ye, L.; Clarkson, J. D.; Wang, C.; Liu, J.; Salahuddin, S.; Ralph, D. C.; Schlom, D. G.; Iniguez, J.; Huey, B. D.; Ramesh, R. *Nature* **2014**, *516*, 370.
- (20) Mostovoy, M. *Nat. Mater.* **2010**, *9*, 188.
- (21) Fukami, S.; Zhang, C.; Dutta Gupta, S.; Kurenkov, A.; Ohno, H. *Nat. Mater.* **2016**, *15*, 535.

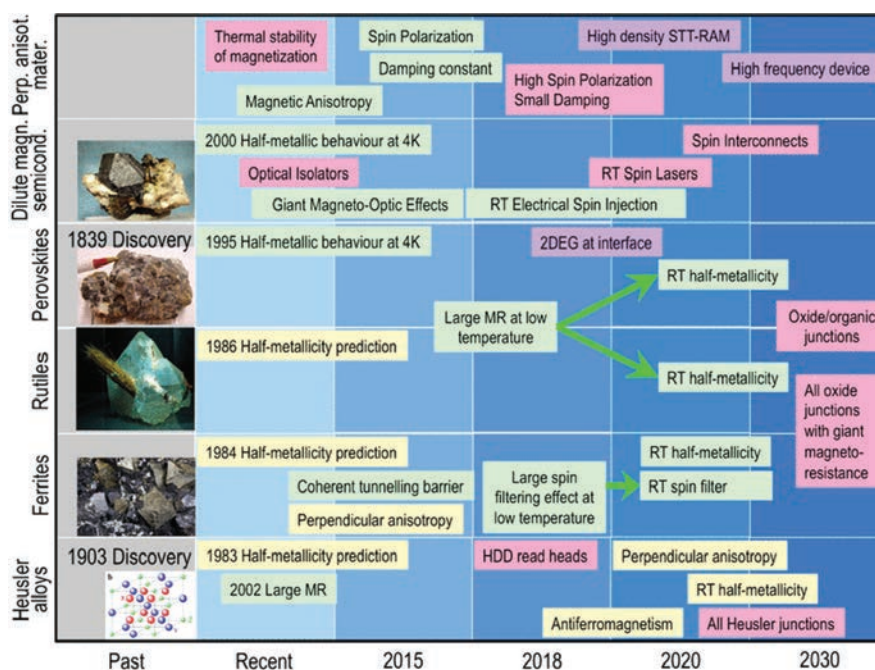


Figure 4. Roadmap for magnetic spintronic materials. Copyright: *IEEE Transactions on Magnetics*³

Substrates for Thin Film Deposition

For a complete list of available materials, visit aldrich.com/substrates.

Name	Composition	Dimensions	Orientation	Prod. No.
Aluminum oxide	Al ₂ O ₃	L × W × thickness 10 × 10 × 0.5 mm	<0001>	634875-1EA 634875-5EA
Gallium antimonide	GaSb	diam. × thickness 2 in. × 0.5 mm	<100>	651478-1EA
Gallium arsenide	GaAs	diam. × thickness 2 in. × 0.5 mm	<100>	651486-1EA
Gallium phosphide	GaP	diam. × thickness 2 in. × 0.5 mm	<111>	651494-1EA
Lanthanum aluminum oxide	LaAlO ₃	10 × 10 × 0.5 mm	<100>	634735-1EA
LSAT	(LaAlO ₃) ₃ (Sr ₂ AlTaO ₆) ₇	10 × 10 × 0.5 mm	<100>	635050-1EA
Magnesium aluminate	MgO·Al ₂ O ₃	L × W × thickness 10 × 10 × 0.5 mm	<100>	635073-1EA
	MgO·Al ₂ O ₃	10 × 10 × 0.5 mm	<110>	634840-1EA
	MgO·Al ₂ O ₃	10 × 10 × 0.5 mm	<111>	634832-1EA
Magnesium oxide	MgO	L × W × thickness 10 × 10 × 0.5 mm	<100>	634646-1EA
Silicon dioxide	SiO ₂	L × W × thickness 10 × 10 × 0.5 mm	<0001>	634867-5EA
Strontium titanate	SrTiO ₃	10 × 10 × 0.5 mm	<111>	638161-1EA
	SrTiO ₃	10 × 10 × 0.5 mm	<100>	634689-1EA
Titanium(IV) oxide, rutile	TiO ₂	L × W × thickness 10 × 10 × 0.5 mm	<001>	635057-1EA
	TiO ₂	L × W × thickness 10 × 10 × 0.5 mm	<100>	635049-1EA
	TiO ₂	L × W × thickness 10 × 10 × 0.5 mm	<110>	635065-1EA

Sputtering Targets

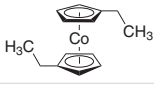
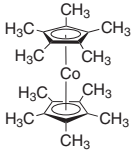
For a complete list of available materials, visit aldrich.com/pvd.

Name	Diam. × Thickness (in.)	Purity (%)	Prod. No.
Aluminum	3.00 × 0.125	99.9995	749036-1EA
Chromium	3.00 × 0.125	99.95	749052-1EA
Nickel	2.00 × 0.25	99.95	767484-1EA
Silicon	2.00 × 0.25	99.999	767492-1EA
Tantalum	2.00 × 0.25	99.95	767514-1EA
Titanium	3.00 × 0.125	99.995	749044-1EA
	2.00 × 0.25	99.995	767506-1EA
Tungsten	2.00 × 0.25	99.95	767522-1EA
Yttrium(III) oxide	2.00 × 0.25	99.99	774022-1EA
Yttrium sputtering target	2.00 × 0.25	99.9	773972-1EA
Zinc	3.00 × 0.125	99.995	749060-1EA

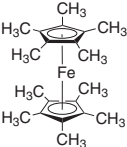
Vapor Deposition Precursors for Magnetic Thin Film Formation

For a complete list of available materials, visit aldrich.com/vapordeposition.

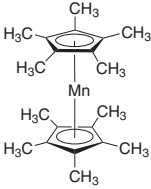
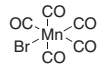
Cobalt

Name	Structure	Form	Prod. No.
Bis(cyclopentadienyl)cobalt(II)		solid powder or crystals	339164-2G 339164-10G
Bis(ethylcyclopentadienyl)cobalt(II)		liquid	510645-1G
Bis(pentamethylcyclopentadienyl)cobalt(II)		solid	401781-1G

Iron

Name	Structure	Purity (%)	Prod. No.
Bis(pentamethylcyclopentadienyl)iron(II)		97%	378542-1G 378542-5G
Iron(0) pentacarbonyl	$\text{Fe}(\text{CO})_5$	>99.99% trace metals basis	481718-25ML 481718-100ML

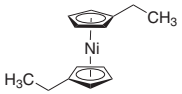
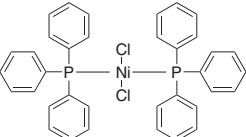
Manganese

Name	Structure	Purity (%)	Prod. No.
Bis(pentamethylcyclopentadienyl)manganese(II)		-	415405-1G
Bromopentacarbonylmanganese(I)		98%	341622-5G
Cyclopentadienylmanganese(I) tricarbonyl		-	288055-1G
Manganese(0) carbonyl	$\text{Mn}_2(\text{CO})_{10}$	98%	245267-1G 245267-10G

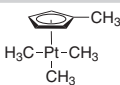
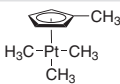
Molybdenum

Name	Structure	Purity (%) Or Grade,	Prod. No.
Molybdenumhexacarbonyl	$\text{Mo}(\text{CO})_6$	$\geq 99.9\%$ trace metals basis	577766-5G 577766-25G
	$\text{Mo}(\text{CO})_6$	98%	199958-10G 199958-50G 199958-250G
	$\text{Mo}(\text{CO})_6$	technical grade	69875-5G 69875-25G 69875-100G

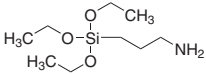
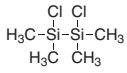
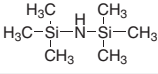
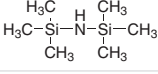
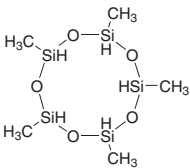
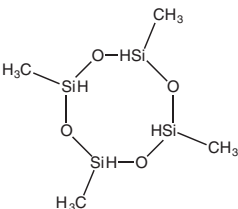
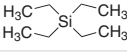
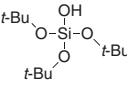
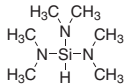
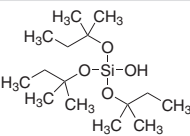
Nickel

Name	Structure	Form	Prod. No.
Bis(cyclopentadienyl)nickel(II)		solid	N7524-5G
Bis(ethylcyclopentadienyl)nickel(II)		liquid	510483-5G
Bis(triphenylphosphine)nickel(II) dichloride		-	529621-10G

Platinum

Name	Structure	Form	Prod. No.
Trimethyl(methylcyclopentadienyl)platinum(IV)		low-melting solid	645605-2G
		low-melting solid	697540-10G

Silicone

Name	Structure	Purity (%)	Prod. No.
(3-Aminopropyl)triethoxysilane		≥98.0%	741442-100ML 741442-500ML
1,2-Dichlorotetramethyldisilane		95%	415456-5ML
Hexamethyldisilazane		99.9%	379212-25ML 379212-100ML
		≥99%	440191-100ML 440191-1L
2,4,6,8,10-Pentamethylcyclopentasiloxane		96%	517801-25ML
2,4,6,8-Tetramethylcyclotetrasiloxane		≥99.5% ≥99.999% trace metals basis	512990-25ML 512990-100ML
Silicon tetrabromide	SiBr ₄	99.995% trace metals basis 99%	494100-5ML 494100-25ML 333468-10G
Silicon tetrachloride	SiCl ₄	99.998% trace metals basis 99.998% trace metals basis 99%	289388-100ML 289388-800ML 688509-25ML 215120-100G 215120-1KG
Tetraethylsilane		99%	510874-5ML
Tetramethylsilane		≥99.99% trace metals basis	523771-100ML
Tris(<i>tert</i> -butoxy)silanol		99.999%	553468-5G 553468-25G
Tris(dimethylamino)silane		>99.9%	759562-25G
Tris(<i>tert</i> -pentoxysilanol		≥99.99%	553441-5G 553441-25G

SOFT MAGNETIC NANOCRYSTALLINE ALLOYS: MATERIALS AND MODELS



Victorino Franco
Departamento de Física de la Materia Condensada, ICMSE-CSIC
Universidad de Sevilla, P.O. Box 1065, 41080, Sevilla, Spain
Email: vfranco@us.es

Introduction

Magnetic materials permeate numerous daily activities in our lives.¹ They are essential components of a diversity of products including hard drives that reliably store information on our computers, decorative magnets that keep the shopping list attached to the refrigerator door, electric bicycles that speed our commute to work, as well as wind turbines for conversion of wind energy to electrical power. While permanent magnets require materials that maintain their magnetization even under the influence of external stimuli, soft magnetic materials can easily change their magnetization when external conditions require it. Permanent magnets require the magnetization vs. field hysteresis loop, $\mathbf{M}(\mathbf{H})$, to be broad, with a large coercive field in order to allow energy to be stored in the material. In contrast, soft magnetic materials require a narrow hysteresis loop, which implies the use of small amounts of energy to magnetize the material. As the area of the loop is related to energy losses during the cyclic magnetization of the material, a low coercive field implies better energy efficiency of the final application in which the soft magnetic material is used.

In addition to saturation magnetization (\mathbf{M}_s), the most relevant properties of soft magnetic materials are the coercive field (\mathbf{H}_c) and the magnetic permeability (μ_r). Maximizing \mathbf{M}_s and μ_r uses less material to achieve the same value of magnetic moment (\mathbf{M}) and a larger response to the excitation field (μ_r). In contrast, optimized soft magnetic materials have the lowest possible value of \mathbf{H}_c . From a practical point of view, large values of μ_r imply that permeability and susceptibility (χ) are interchangeable for the purpose of describing the properties of the material, expressed as $\mu_r = 1 + \chi \approx \chi$. In addition, large susceptibility requires additional attention when characterizing the magnetic material. The magnetic field sensed by the sample, the internal field \mathbf{H}_i , is not directly the applied field \mathbf{H}_a , but rather depends on the demagnetizing factor (\mathbf{N}) of the sample: $\mathbf{H}_i = \mathbf{H}_a - \mathbf{N}\mathbf{M}$. If we disregard the difference between internal

and applied fields and we consider that the apparent susceptibility of the sample (χ_a) associates magnetization and applied field (instead of relating magnetization and internal field, which stands for the intrinsic susceptibility of the material, χ) we obtain:

$$\chi_a = \frac{\chi}{1 + \mathbf{N}\chi} \quad (1)$$

Therefore, for samples with large values of \mathbf{N} made of materials with a large value of χ , the apparent susceptibility does not depend on the actual value of the susceptibility of the material, but only on the demagnetizing factor, as: $\chi_a \approx 1/\mathbf{N}$ (Equation 2).

Thus, the measurement is exclusively dependent on the shape of the sample. To avoid this artifact, geometries that minimize \mathbf{N} , such as long wires magnetized along their axis, planar samples magnetized in plane, or toroids magnetized along the toroidal direction are best used. As a direct consequence of Equation 2, the internal field is cancelled, shielding the magnetic field from a spatial region. In fact, a cage made using a soft magnetic material with large susceptibility provides a path for the magnetic field, minimizing its value in the interior of the cage. This explains why mu-metal®, with relative permeability values on the order of 500,000, is used in this type of application.

Scientific publications on soft magnets have steadily increased over the past decades. For example, the discovery of the alloy FINEMET® with its outstanding soft magnetic properties has made the field more attractive to researchers.² A comparison between the number of papers published on soft magnets to those on hard, or permanent magnets (Figure 1), shows the latter field has been more active in recent years. The accelerating research on soft magnetic nanocrystalline materials in Asia is considered a major driver of growth in the field. This heightened interest has generated an increased demand for and consumption of electrical steel since 2008, promoting the installation of new transformers to improve grid reliability and reduce energy losses. The connection between energy efficiency and soft magnets will help to move soft magnetic nanocrystalline alloy research back into the forefront in the future.

This article provides a brief overview of soft magnetic nanocrystalline alloys. As indicated above, a main goal of optimizing these materials is to obtain the lowest possible coercivity. Here, we review the most important families of nanocrystalline soft magnets with a description of their typical properties and how their composition and processing allow the optimization of these properties. Finally, we present an outlook of potential future fields of interest.

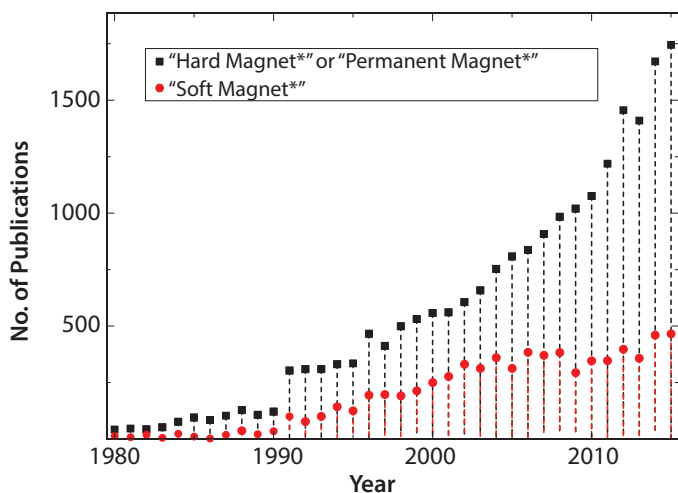


Figure 1. Evolution of the number of publications appearing in *Science Citation Index Expanded* on soft magnetic materials and permanent magnets since 1980. The search string used for the search is provided in the labels.

Desired Properties

The dependence of coercivity on crystal size exhibits two different behavioral regimes. The traditional method of decreasing coercivity in soft magnetic materials has historically been to increase grain size because this decreases the amount of grain boundaries that act as pinning centers for the domain walls. By increasing grain size from 100 nm to 100 μm , it is possible to decrease H_c from $\sim 10,000$ A/m to values on the order of 1 A/m. The counter-example of this approach appeared with the emergence of amorphous and nanocrystalline materials. By decreasing grain size to values on the order of 10 nm or even making the solid amorphous, coercivity decreases to reach values comparable to those of very large crystals. Taking into account that an amorphous structure is, by definition, full of defects, the previous argument of decreasing coercivity with decreasing concentration of defects no longer holds true. This characteristic behavior can be explained with the Random Anisotropy Model (RAM) of Alben, Becker, and Chi³ and has been applied to nanocrystalline alloys by Herzer.⁴

Random Anisotropy Model: An Explanation Based on Analogies

A formal explanation of the RAM remains elusive for researchers more interested in material properties than in the development of physical models. However, understanding the physics behind the model can help in designing materials with the desired performance. We use several analogies taken from everyday life to grasp the concept of RAM. The message here is that the existence of very different length scales in the sample is responsible for the vanishing effective anisotropy of the amorphous and nanocrystalline alloys, which gives rise to extremely low coercivity values.

The first example takes us on a walk to a traditional monument found in many old cities, like Sevilla. Many of these ancient cities have patios with a floor made of numerous pebbles. When walking on top of these floors, those wearing high heels will typically have more difficulty walking than those wearing flat-soled shoes. The most reasonable explanation for this circumstance is that high heels have a typical size comparable to the pebbles and the gaps between them so they detect the discrete maximum and minimum heights of the floor. Flat shoes average the irregularities and allow us to walk more steadily because the heel is much longer than the pebbles and gaps.

Another example uses two refrigerator magnets with the same characteristics (ideally, two identical ones). Magnets of this type are fabricated using polymer-bonded ferromagnetic particles with a domain structure consisting of a set of stripes pointing outward and inward on one side, with the other side containing closure domains. The side with the closure domains is typically decorated and will not stick to the fridge. When one magnet is placed directly on top of the other with the same orientation (decorated sides facing the exterior), the magnets stick together. However when one magnet is slid perpendicular to the stripe domain, the upper magnet jumps as it moves along the attractive and repulsive regions with a periodicity corresponding to twice the domain width. As both the upper and lower magnets have the same characteristic length, i.e., the width of the domains, the system samples energy maxima and minima and they are detected macroscopically. This can be felt in our hands when trying to move the magnets, often producing a sound due to the abrupt attaching and detaching of the flexible laminae. However, if we rotate the upper magnet 90° with respect to the lower magnet, in a perpendicular orientation of the stripe domains of both laminae, the movement in any direction becomes smooth. It is not because the local maxima and minima have disappeared. There are still regions where equal poles face each other and therefore repel, as well as areas in which opposite poles lie on top of each other, creating attraction. The difference with respect to the previous situation is that any position of the upper magnet samples the same amount of attractive and repelling areas. The periodicity of the lower magnet remains the width of the domains, while the periodicity of the upper magnet turns to the length of the magnet. As one is much larger than the other, we cannot macroscopically detect the local energy difference and the magnets displace smoothly, similar to the flat-soled shoes on the pebbled patio.

A Simple Model for Nanocrystalline Alloys

Nanocrystalline alloys also can be modeled in a simple fashion as an ensemble of single domain nanoparticles (shown as squares in **Figure 2A**) with a typical grain size of 10 nm and with randomly oriented easy axes. Even if Fe-based nanocrystals have cubic magnetocrystalline anisotropy, we consider uniaxial anisotropy in the current model. We will show that the effective anisotropy is almost averaged to zero, thus this assumption of symmetry does not affect our conclusion. Consider the case in which the domain size (connected to the magnetic correlation length and marked as a thick white square in **Figure 2B**) is comparable to the structural correlation length (the grain size in **Figure 2A**). Assuming we have a domain in which the magnetization is oriented in the horizontal direction inside the white square, we color code the anisotropy energy of the different crystals from blue (minimal anisotropy energy) to red (maximal anisotropy energy). It is easy to see in the figure that it is not equivalent to displace this domain in all directions, since in some cases we gain blue squares (when moving to the right), while we don't notice a remarkable difference in red or blue when moving up because there is anisotropy in the displacement of the domain. When we progressively decrease grain size while keeping the domain size constant, differences in energy will become gradually smaller when we move the domain in any direction, becoming negligible below a certain grain size. Each grain has its own anisotropy energy, but the system as a whole does not present anisotropy. In order to perform this simulation more quantitatively, we create different grids using different ratios of grain size to domain size and place the correlated domain at all positions in the grid, calculating the total value of energy in each position and the difference between maximal and minimal energy values for each of the grids. When we plot the difference in energy as a function of the number of particles inside each domain, N , we clearly observe a decreasing trend that can be fit to a $1/\sqrt{N}$ law. Taking into account, for this model, anisotropy is a function of the difference in energy for each position of the domain inside the grid, we observe that the effective anisotropy, K^* , corresponds to $K^* = K/\sqrt{N}$, where K is the anisotropy of the crystals. This is the same result formally

obtained from the RAM and originates from the difference between the magnetic correlation length and the structural correlation length. As a consequence of this discussion, when particle size decreases noticeably below the exchange correlation length, the effective anisotropy decreases toward zero and makes coercivity practically null.

This simplistic explanation, while keeping the essence of the phenomenology, was improved by also considering nanocrystalline alloys are not only formed by the nanocrystals, but they are two-phase systems in which the nanocrystals are embedded in a residual amorphous matrix, which is also ferromagnetic. More sophisticated models for multiphase materials have been developed^{5,6} that also include the contributions of magnetoelastic energy.

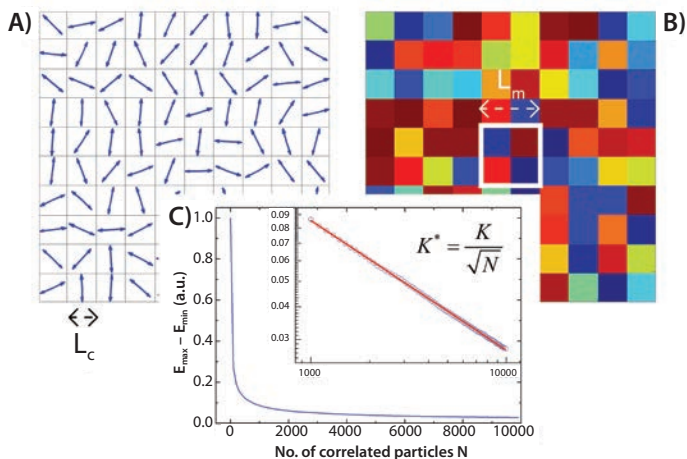


Figure 2. A) Set of L_c -sized particles with randomly oriented uniaxial anisotropy. B) Color-coded energy of such crystals if their magnetization is horizontal, showing one particular size of the magnetic correlation length L_m . C) Relative differences in energy of the correlated region when placed in all different areas of the ensemble, as a function of the number of crystals inside the correlated region (by altering the L_m/L_c ratio); inset: logarithmic plot and linear fit to the data, showing $1/\sqrt{N}$ dependence.

Soft Magnetic Nanocrystalline Alloys

As indicated in the previous section, obtaining materials in which the exchange correlation length is much larger than the structural correlation length will lead to effective magnetic anisotropies that are negligible when compared to the magnetocrystalline anisotropy of the bulk material. In practice, this can be achieved by controlled crystallization of a precursor amorphous alloy.

A major breakthrough in this research field took place with the discovery of the FINEMET[®] alloy by Yoshizawa, Oguma and Yamaguchi in 1988.² This alloy is formed from Fe, Si, and B, with small additions of Cu and Nb, and has a typical alloy composition of $Fe_{73.5}Si_{13.5}B_9Cu_1Nb_3$. The alloy is usually fabricated using rapid solidification techniques such as melt spinning in order to obtain an amorphous precursor with the desired composition. At this stage of the fabrication process, the role of B is to increase the glass-forming ability of the precursor alloy. Subsequently, the obtained ribbons are submitted to controlled annealing, typically 1 h at temperatures on the order of 500 °C in order to obtain the desired microstructure of α -FeSi nanocrystals with a typical grain size of 10 nm embedded in a residual ferromagnetic amorphous matrix. The role of Cu is to favor the nucleation of the nanocrystals via segregation either prior to or at the early stages of nanocrystallization. Conversely, the slow diffusing Nb accumulates at the boundaries of the emerging nanocrystals and hinders grain growth.

This special microstructure creates the optimal soft magnetic properties found in this type of alloy; the nanocrystals couple magnetically through the amorphous ferromagnetic matrix in which they are embedded, making the magnetic correlation length much larger than the size of the nanocrystals and averaging the magnetocrystalline anisotropy down to zero. Nevertheless, magnetocrystalline anisotropy is not the only source of coercivity. Magnetoelastic anisotropy also plays an important role. However, the different sign of the saturation magnetostriction constant of the two ferromagnetic phases (negative for the nanocrystals, positive for the amorphous matrix) means that, for a proper amount of the crystalline fraction, this source of anisotropy also vanishes. This makes FINEMET one of the softest materials known to date, with coercivities under 1 A/m. Compositional variations of the alloy produce slightly different Si content in the nanocrystals, altering the value of their magnetostriction constant. This modifies the overall magnetic anisotropy and alters either the optimal crystalline fraction to minimize coercivity, or prevents the overall magnetostriction from vanishing.⁷

The dependence of coercivity on annealing temperature, i.e., changing microstructure, is illustrated in **Figure 3**.⁸ As cast, the amorphous alloy is considered soft for most applications. Annealing at temperatures below the first crystallization stage produces a decrease of coercivity due to stress relaxation processes, diminishing magnetoelastic anisotropy. The appearance of the first nanocrystals increases coercivity by acting as pinning centers for the domain walls and by inducing new stresses in the sample. Increasing annealing temperature further increases the crystalline volume fraction. When the fraction is large enough, the nanocrystals are magnetically coupled through the ferromagnetic amorphous matrix, averaging the magnetocrystalline anisotropy according to the random anisotropy model extended to two-phase systems.^{5,6} Finally, the onset of the second crystallization stage, with the precipitation of highly anisotropic iron boride type phases, increases coercivity to such an extent the material is of no use as a soft magnet.

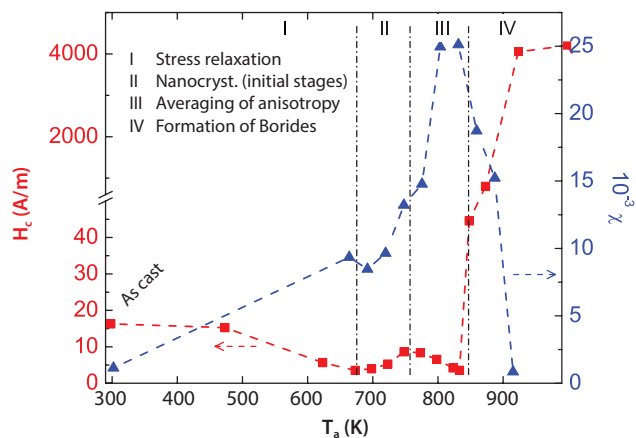


Figure 3. Annealing temperature dependence of room temperature coercivity and initial susceptibility of $Fe_{76}Cu_1Nb_3Si_{10.5}B_{9.5}$ alloy.

Fabrication and Processing

The most common methods for obtaining nanocrystalline microstructure include either conventional annealing in a furnace or Joule-heating/flash annealing, i.e., passing a current through a sample in order to heat it in a controlled fashion. The latter method has been proven useful in reducing the brittleness of the nanocrystalline samples⁹ and is also combined with the simultaneous application of mechanical stress.¹⁰ Processing the alloy under the combined effect of temperature and magnetic field is also

useful for inducing anisotropy in the alloys and, therefore, controlling the shape of the hysteresis loop, making them more appropriate for certain applications.^{11–13}

Although there have been attempts to produce these ultra-soft nanocrystalline alloys using mechanical alloying of pure elemental powders, the coercivity of these powders is considerably higher than that obtained for ribbon-shaped samples.¹⁴ The increase in magnetoelastic anisotropy due to the additional microstrains and the reduced mobility of domain walls as a result of the size of the powder particles are the main causes of the increased coercivity. It is also important to consider the difficulties in incorporating B into the alloy, despite starting from amorphous or crystalline B powders.¹⁵

Compositional Effects

In recent years, there have been numerous studies on the influence of composition on the soft magnetic properties of amorphous and nanocrystalline alloys. Due to the necessary brevity of this paper, the reader is referred to the literature for more comprehensive reviews.^{16,17} In addition to the FINEMET® alloy and its variations already mentioned in this paper, the three most relevant families of nanocrystalline alloys for soft magnetic applications are NANOPERM®, HITPERM, and NANOMET®. NANOPERM alloys have a typical composition of $\text{Fe}_{88}\text{Zr}_7\text{B}_4\text{Cu}_1$.^{18,19} The larger Fe content and the lesser amount of B increases its saturation magnetization with respect to FINEMET alloys. The nanocrystalline phase consists in α -Fe, in contrast to the FINEMET alloy which also contained Si in the nanocrystals. This has made these alloys a preferred system for the study of the nanocrystallization process via Mossbauer spectroscopy.²⁰

HITPERM alloys were designed as high-temperature soft magnetic materials.²¹ Their original composition was $\text{Fe}_{44}\text{Co}_{44}\text{Zr}_7\text{B}_4\text{Cu}$, in which Co serves two purposes. On one hand, it helps to maximize the magnetic moment, as Fe-Co alloys are at the top of the Slater-Pauling curve. On the other hand, Co increases the Curie temperature of both the residual amorphous phase and the nanocrystals (which are α -FeCo and α' -FeCo) and allows the operation of HITPERM alloys at much larger temperatures than the other families. But for high temperature applications, the challenge is not only connected to the Curie temperature of the phases, but since we are dealing with metastable materials, we also have to take into account the temperature at which microstructural transformation will take place. This family of alloys fulfills both requirements.

The latest addition to the families of soft magnetic nanocrystalline alloys is the NANOMET alloy, with typical composition $\text{Fe}_{83.3-84.3}\text{Si}_4\text{B}_8\text{P}_{3-4}\text{Cu}_{0.7}$.²² NANOMET was developed to increase the saturation magnetization and minimize material cost by reducing or eliminating the metallic additions of Nb, Zr, Mo, and Cu which were usually required in the alloy families in order to achieve the nanocrystalline microstructure. These nanocrystalline alloys show high saturation magnetization, comparable to the commercial Fe-Si crystalline soft magnetic alloys, and low coercivity.

Regardless of the alloy family, nanocrystalline soft magnets must be optimized for specific operating conditions. A material with good performance at room temperature will most likely not be suitable for cryogenic applications. Cryogenic application studies of the compositional effects in the (Fe,Si,Al)NbBCu alloy series show that proper selection of the Fe:Si:Al ratio allows for the optimal combination of high saturation magnetization, low coercivity, and large electrical resistivity at liquid nitrogen temperatures.²³ In another recent example, the Curie temperature of amorphous and nanocrystalline alloys was tuned by compositional variation of the Co:Ni ratio in the $\text{Fe}_{88.2x}\text{Co}_x\text{Ni}_x\text{Zr}_7\text{B}_4\text{Cu}_1$

alloy series with the aim of analyzing the potential of Fe-based amorphous alloys for room temperature magnetic refrigeration.²⁴ The $\text{Fe}_{88-2x}\text{Co}_x\text{Ni}_x\text{Zr}_7\text{B}_4\text{Cu}_1$ alloy series exhibits the largest refrigerant capacity (RC) of Fe-based amorphous alloys found to date, while still keeping one of the largest magnetic entropy changes among Fe-based amorphous alloys. For magnetic refrigeration, it appears that nanocrystalline Fe-based²⁵ and Ni-based²⁶ alloys are not suitable and amorphous alloys are preferred, since the magnetic entropy change peak of the two-phase nanocrystalline alloys is split between the magnetic phase transition of the amorphous phase and that of the nanocrystals, decreasing its total magnitude.²⁷

In addition to their use as soft magnets, ultra-soft magnetic materials can be combined with other materials for the development of exchange-coupled nanocomposite permanent magnets, in which a nanoscale soft magnetic phase is added into a hard magnetic phase matrix, increasing the energy density of the composite due to interphase exchange coupling.²⁸

Nevertheless, the scientific interest in soft magnetic nanocrystalline alloys is not only driven by their technological applications and potential to increase energy efficiency. Their two-phase nature, with magnetic phases with different Curie temperatures, makes them a good testing ground for conducting fundamental studies in magnetism. Soft magnetic nanocrystalline alloys have been used to study the superparamagnetism of nanocrystals embedded in the matrix²⁹ in order to develop models of the dipolar interactions between superparamagnetic nanoparticles^{30–33} or to propose procedures for the determination of critical exponents of multiphase magnetic systems.²⁶

Conclusions and Outlook

Nanocrystalline alloys are among the softest magnetic materials known to science, and different alloy families have been optimized for unique applications and operating conditions. In addition to compositional effects that will affect intrinsic magnetic properties, the use of different processing methods enables the optimization of extrinsic properties such as coercivity.

The physical reason for the extremely low values of magnetic anisotropy and coercive field can be explained using the random anisotropy model: the two characteristic length scales of nanocrystalline alloys (grain size and magnetic correlation length) are very different, and anisotropy cannot be detected macroscopically, even if each nanocrystal is anisotropic.

Soft magnets are currently used in a variety of applications, ranging from energy conversion to sensors. Remaining challenges in the development of soft magnetic nanocrystalline alloys include the optimization of material properties for specific applications and the enhancement of their usability by decreasing brittleness and increasing thermal stability of the metastable phases. These goals can be achieved by a combination of compositional changes and appropriate processing of the alloys. Tuning the hysteresis loops by processing the materials under the simultaneous influence of magnetic field, stress, and temperature is a promising route to broadening the applications of nanocrystalline soft magnets. In addition, the design of exchange-coupled hard-soft magnetic nanocomposites is an area of significant interest in which ultrasoft nanocrystalline alloys may play a role. Moreover, the interest in soft nanocrystalline alloys is not limited to technological applications as these materials are also a good testing ground for developing fundamental models of multiphase magnetic materials.

Acknowledgments

This work was supported by MINECO and EU FEDER (project MAT2016-77265-R) and the PAI of the Regional Government of Andalucía.

References

- (1) Gutfleisch, O.; Willard, M. A.; Bruck, E.; Chen, C. H.; Sankar, S. G.; Liu, J. P. *Adv. Mater.* **2011**, *23*, 821–842.
- (2) Yoshizawa, Y.; Oguma, S.; Yamauchi, K. *J. Appl. Phys.* **1988**, *64*, 6044–6046.
- (3) Alben, R.; Becker, J. J.; Chi, M. C. *J. Appl. Phys.* **1978**, *49*, 1653–1658.
- (4) Herzer, G. *IEEE T Magn.* **1990**, *26*, 1397–1402.
- (5) Suzuki, K.; Cadogan, J. M. *Phys. Rev. B* **1998**, *58*, 2730–2739.
- (6) Hernando, A.; Vazquez, M.; Kulik, T.; Prados, C. *Phys. Rev. B* **1995**, *51*, 3581–3586.
- (7) Franco, V.; Conde, C. F.; Conde, A. *J. Appl. Phys.* **1998**, *84*, 5108–5113.
- (8) Franco, V.; Conde, C. F.; Conde, A.; Kiss, L. F. *J Magn Magn. Mater.* **2000**, *215–216*, 400–403.
- (9) Allia, P.; Tiberio, P.; Baricco, M.; Vinai, F. *Appl. Phys. Lett.* **1993**, *63*, 2759–2761.
- (10) Aranda, G. R.; Gonzalez, J.; Kulakowski, K.; Echeberria, J. J. *Appl. Phys.* **2000**, *87*, 4389–4394.
- (11) Appino, C.; Beatrice, C.; Coisson, M.; Tiberio, P.; Vinai, F. *J Magn. Magn. Mater.* **2001**, *226*, 1476–1477.
- (12) Skorvanek, I.; Marcin, J.; Turcanova, J.; Wojcik, M.; Nesteruk, K.; Janickovic, D.; Svec, P. *J Magn. Magn. Mater.* **2007**, *310*, 2494–2496.
- (13) Blazquez, J. S.; Marcin, J.; Varga, M.; Franco, V.; Conde, A.; Skorvanek, I. *J. Appl. Phys.* **2015**, *117*, 17A301.
- (14) Blázquez, J. S.; Ipus, J. J.; Lozano-Pérez, S.; Conde, A. *Jom-U.S.* **2013**, *65*, 870–882.
- (15) Ipus, J. J.; Blázquez, J. S.; Conde, C. F.; Borrego, J. M.; Franco, V.; Lozano-Perez, S.; Conde, A. *Intermetallics* **2014**, *49*, 98–105.
- (16) McHenry, M. E.; Willard, M. A.; Laughlin, D. E. *Prog. Mater. Sci.* **1999**, *44*, 291–433.
- (17) Willard, M. A.; Daniil, M. in *Nanoscale Magnetic Materials and Applications*, edited by J. Ping Liu, Eric Fullerton, Oliver Gutfleisch et al. (Springer, New York, **2009**), pp. 373–397.
- (18) Suzuki, K.; Makino, A.; Kataoka, N.; Inoue, A.; Masumoto, T. *Materials Transactions, JIM* **1991**, *32*, 93–102.
- (19) Makino, A.; Hatanai, T.; Inoue, A.; Masumoto, T. *Mat. Sci. Eng. a-Struct.* **1997**, *226*, 594–602.
- (20) Kemeny, T.; Kaptas, D.; Kiss, L. F.; Balogh, J.; Vincze, I.; Szabo, S.; Beke, D. L. *Hyperfine Interact* **2000**, *130*, 181–219.
- (21) Willard, M. A.; Laughlin, D. E.; McHenry, M. E.; Thoma, D.; Sickafus, K.; Cross, J. O.; Harris, V. G. *J. Appl. Phys.* **1998**, *84*, 6773.
- (22) Makino, A.; Men, H.; Kubota, T.; Yubuta, K.; Inoue, A. *Mater. Trans.* **2009**, *50*, 204–209.
- (23) Daniil, M.; Osofsky, M. S.; Gubser, D. U.; Willard, M. A. *Appl. Phys. Lett.* **2010**, *96*, 162504.
- (24) Caballero-Flores, R.; Franco, V.; Conde, A.; Knipling, K. E.; Willard, M. A. *Appl. Phys. Lett.* **2010**, *96*, 182506.
- (25) Franco, V.; Blazquez, J. S.; Conde, C. F.; Conde, A. *Appl. Phys. Lett.* **2006**, *88*, 042505.
- (26) Sánchez-Pérez, M.; Moreno-Ramírez, L. M.; Franco, V.; Conde, A.; Marsilius, M.; Herzer, G. *J. Alloy Compd.* **2016**, *686*, 717–722.
- (27) Franco, V.; Conde, A. *Scripta Mater* **2012**, *67*, 594–599.
- (28) Liu, J. P., in *Nanoscale Magnetic Materials and Applications*, edited by J. Ping Liu, Eric Fullerton, Oliver Gutfleisch et al. (Springer, New York, **2009**), pp. 309–335.
- (29) Slawskawaniewska, A.; Gutowski, M.; Lachowicz, H. K.; Kulik, T.; Matyja, H. *Phys. Rev. B* **1992**, *46*, 14594–14597.
- (30) Allia, P.; Coisson, M.; Tiberio, P.; Vinai, F.; Knobel, M.; Novak, M. A.; Nunes, W. C. *Phys. Rev. B* **2001**, *64*, 144420.
- (31) Allia, P.; Coisson, M.; Knobel, M.; Tiberio, P.; Vinai, F. *Phys. Rev. B* **1999**, *60*, 12207–12218.
- (32) Franco, V.; Kiss, L. F.; Kemeny, T.; Vincze, I.; Conde, C. F.; Conde, A. *Phys. Rev. B* **2002**, *66*, 224418.
- (33) Franco, V.; Conde, C. F.; Conde, A.; Kiss, L. F. *Phys. Rev. B* **2005**, *72*, 174424.

HAVE YOU MISSED OUR RECENT ISSUES?

- Vol. 11 No. 3: Biopolymers for Medicine (SEI)
- Vol. 11 No. 2: Three-dimensional Science (SAL)
- Vol. 11 No. 1: Next Generation Nanomaterials for Energy and Electronics (RYO)
- Vol. 10 No. 4: Biomaterials for Tissue Engineering (RVR)
- Vol. 10 No. 3: Alternative Energy Generation and Storage (RRB)
- Vol. 10 No. 2: Graphene and Carbon Materials (ROM)



To view a complete library of issues or to subscribe to our newsletter, visit aldrich.com/materialmatters

Magnetic Materials

For a complete list of available materials, visit aldrich.com/magnetic.

Oxides

Name	Purity	Particle Size	Form	Prod. No.
Chromium(VI) oxide	99.99% trace metals basis	-	powder or flakes	675644-5G 675644-25G
Cobalt(II) oxide	≥99.99% trace metals basis	-	powder	529443-5G 529443-25G
	-	-325 mesh	powder	343153-10G 343153-100G
Cobalt(II,III) oxide	99.995% trace metals basis	-	calcined	203114-5G
	-	<10 μm	powder	221643-50G 221643-250G
Iron(II) oxide	99.9% trace metals basis	-10 mesh	powder	400866-5G 400866-25G
Iron(II,III) oxide	99.99% trace metals basis	-	powder	518158-10G 518158-50G
	95%	<5 μm	powder	310069-25G 310069-500G 310069-2.5KG
Iron(III) oxide	-	30 - 50 mesh	powder	371254-50G 371254-250G
	≥99.995% trace metals basis	-	powder	529311-5G 529311-25G
Manganese(II) oxide	≥99.99% trace metals basis	-	powder and chunks	431761-1G 431761-10G
	99%	-60 mesh	powder	377201-500G
Manganese(II,III) oxide	97%	-	powder	377473-100G
Manganese(III) oxide	99.9% trace metals basis	-	solid	463701-5G 463701-25G
	99%	-325 mesh	powder	377457-250G 377457-1KG
Manganese(IV) oxide	≥99.99% trace metals basis	-	powder and chunks	529664-5G 529664-25G
Nickel(II) oxide	≥99.995% (Trace Metals Analysis)	-	solid	481793-5G 481793-25G

Alloys

Name	Composition	Size (L x W) (mm)	Form	Prod. No.
Aluminum nickel cobalt	Al / Ni / Co	13 × 6	disc	692867-2EA
	Al / Ni / Co	13 × 6	disc	692875-3EA
Aluminum-scandium alloy	Al / Sc	-	ingot	755672-1EA
Neodymium-iron-boron alloy 30/150	Nd / Fe / B	13 × 6	disc	693782-3EA
Samarium-cobalt alloy 18	SmCo ₅	10 × 6	disc	692859-3EA
Samarium-cobalt alloy 24	Sm ₂ Co ₁₇	10 × 6	disc	692840-3EA
Samarium-cobalt alloy 30	Sm ₂ Co ₁₇	10 × 6	disc	692832-3EA
Woods metal	Bi / Pb / Cd / Sn	-	granular	95430-100G 95430-500G

Nanomaterials

For a complete list of available materials, visit aldrich.com/nanomagnetic.

Name	Composition	Purity (% trace metals basis)	Particle Size (nm)	Form	Prod. No.
Barium ferrite	BaFe ₁₂ O ₁₉	>97	particle size <100 (BET)	nanopowder	637602-25G
Bismuth cobalt zinc oxide	(Bi ₂ O ₃) _{0.07} (CoO) _{0.03} (ZnO) _{0.90}	99.9	particle size <50 (XRD)	nanopowder	631930-5G
Cobalt	Co	≥99	particle size <50 (TEM)	nanopowder	697745-500MG
Cobalt aluminum oxide	CoAl ₂ O ₄	≥99	particle size <50 (BET)	nanopowder	633631-25G
Cobalt iron oxide	CoFe ₂ O ₄	99	particle size 30 (TEM)	nanopowder	773352-5G
Cobalt(II,III) oxide	Co ₃ O ₄	99.5	particle size <50 (TEM)	nanopowder	637025-25G
					637025-100G
					637025-250G

Magnetic Materials: Nanomaterials (cont.)

Name	Composition	Purity (% trace metals basis)	Particle Size (nm)	Form	Prod. No.
Dysprosium(III) oxide	Dy ₂ O ₃	99.9	particle size <100 (BET)	nanopowder	637289-25G
	Dy ₂ O ₃	≥99.9	particle size <50 (XRD)	dispersion	639664-25ML
Erbium(III) oxide	Er ₂ O ₃	≥99.9	particle size <100 (BET)	nanopowder	637343-10G 637343-50G
	Er ₂ O ₃	≥99.9	particle size <100 (BET)	dispersion	641839-100ML
Europium(III) oxide	Eu ₂ O ₃	99.5	particle size <150 (TEM)	nanopowder	634298-25G
Gadolinium(III) oxide	Gd ₂ O ₃	99.8	particle size <100 (BET)	nanopowder	637335-10G 637335-50G
Holmium(III) oxide	Ho ₂ O ₃	≥99.9	avg. part. size <100 (DLS)	nanopowder	637327-10G 637327-50G
	Ho ₂ O ₃	≥99.9	particle size <50 (XRD)	dispersion	641863-25ML
Iron	Fe	99.5	particle size 35–45	nanopowder	746843-5G
	Fe	99.5	avg. part. size 25	nanopowder	746827-5G
	Fe	99.5	avg. part. size 25	nanopowder	746835-5G
	Fe	≥99	particle size 60–80	nanopowder	746878-25G
	Fe	99	particle size 40–60	nanopowder	746851-25G
Iron-nickel alloy	-	≥97	particle size <100 (BET)	nanopowder	677426-5G
Iron nickel oxide	Fe ₂ O ₃ /NiO	≥98	particle size <50 (APS)	nanopowder	637149-25G 637149-100G
Iron(II,III) oxide	Fe ₃ O ₄	97	particle size 50–100 (SEM)	nanopowder spherical	637106-25G 637106-100G 637106-250G
Iron oxide(II,III), magnetic nanoparticles solution	Fe ₃ O ₄	-	avg. part. size 10	solution	700312-5ML
	Fe ₃ O ₄	-	avg. part. size 5	solution	700320-5ML
	Fe ₃ O ₄	-	avg. part. size 20	solution	700304-5ML
Iron(III) oxide	Fe ₂ O ₃	-	particle size <50 (BET)	nanopowder	544884-5G 544884-25G
Iron(III) oxide, dispersion	Fe ₂ O ₃	-	avg. part. size <30 (APS)	nanoparticles	720712-100G
	Fe ₂ O ₃	-	avg. part. size <30 (APS)	nanoparticles	720704-100G
Iron oxide hydroxide	FeOOH	99.5	<5 (DLS)	dispersion	796093-100ML
Neodymium(III) oxide	Nd ₂ O ₃	99.9	particle size <100 (BET)	nanopowder	634611-5G 634611-50G
Nickel	Ni	≥99	avg. part. size <100	nanopowder	577995-5G
Nickel cobalt oxide	(NiO)(CoO)	99	particle size <150 (BET)	nanopowder	634360-25G
Nickel nanowires	-	-	-	powder	745561-500MG
Nickel(II) oxide	NiO	99.8	particle size <50 (TEM)	nanopowder	637130-25G 637130-100G 637130-250G
	NiO	-	-	nanowires	774545-500MG
Nickel zinc iron oxide	NiZnFe ₄ O ₄	≥99	particle size <100 (BET)	nanopowder	641669-10G 641669-50G
Samarium(III) oxide	Sm ₂ O ₃	≥99	particle size <100 (BET)	nanopowder	637319-10G
Samarium(III) oxide dispersion	Sm ₂ O ₃	-	particle size <50 (XRD)	powder	641855-100ML
Samarium strontium cobalt oxide	SrO • Sm ₂ O ₃ • 2Co ₃ O ₄	99.5	particle size <50 (BET)	nanopowder	677442-5G
Terbium(III,IV) oxide	Tb ₄ O ₇	99.5	particle size <100 (BET)	nanopowder	634255-25G
Ytterbium(III) oxide	Yb ₂ O ₃	≥99.7	particle size <100 (BET)	nanopowder	637300-10G
Yttrium aluminum oxide	Y ₃ Al ₅ O ₁₂	99	particle size <150 (TEM)	nanopowder	634638-25G
Yttrium iron oxide	Y ₃ Fe ₅ O ₁₂	99.9	particle size <100 (BET)	nanopowder	634417-10G
Yttrium(III) oxide	Y ₂ O ₃	-	particle size <50	nanopowder	544892-25G
Yttrium(III) oxide, dispersion	Y ₂ O ₃	≥99.9	<100 (DLS)	dispersion nanoparticles	702048-100G

ADDITIVE MANUFACTURING OF PERMANENT MAGNETS



M. P. Paranthaman,¹ I. C. Nlebedim,² F. Johnson,³ S. K. McCall⁴
¹Oak Ridge National Laboratory, Oak Ridge, TN 37831, USA
²Ames Laboratory, Ames, IA 50011, USA
³GE Global Research, Niskayuna, NY 12309, USA
⁴Livermore National Laboratory, Livermore, CA 94550, USA
 Email: paranthamanm@ornl.gov

Introduction

Permanent magnets are an essential technology for energy conversion. Motors and generators are used to convert energy between electrical and mechanical forms. Permanent magnets must be pre-charged (magnetized) prior to their use in an application and must maintain this magnetization during operation. In addition, permanent magnets must generate sufficient magnetic flux for a given application. Nevertheless, permanent magnets can be demagnetized by a number of circumstances, including the presence of other magnetic materials in their service,¹ temperature changes (thermal demagnetization), microstructural degradation, and even the magnet's own internal demagnetizing field. Therefore, the performance of a permanent magnet can be best understood by examining its ability to withstand demagnetization and to supply the magnetic flux required in a given application. Some of these properties are discussed further. Additive manufacturing, followed by exchange spring magnets will be discussed later.

Coercivity

Coercivity is the magnetic field required to reduce the magnetization of a material that is magnetized to saturation down to zero. It is a measure of the ability of a magnetic material to resist demagnetization, i.e., the permanency of a material's magnetization. The term coercivity is often used interchangeably with coercive field, the term for any magnetic field that reduces magnetization to zero whether or not the material was previously magnetized to saturation.

Magnetic materials are classified as hard or soft based on coercivity. Hard magnetic materials such as permanent magnets have high coercivity, while soft magnetic materials such as electrical steel have low coercivity. Coercivity is a structure-sensitive extrinsic magnetic property, affected by temperature, crystal anisotropy, stress-state, and microstructural impurities.² Controlling the properties that affect the structure of permanent magnets is pivotal to the progress that has been made in enhancing coercivity. In permanent magnets, $B = \mu_0(H+M)$, two types of coercivity exist; the field at which the magnetic induction B is zero (H_c) and the field at which magnetization M is zero (intrinsic coercivity, H_{ci}). The former is significantly less than the latter. **Figure 1** shows that rare-earth (RE) permanent magnet alloys based on $Nd_2Fe_{14}B$ (NdFeB or Neo) and RE-Co have very high coercivity.³ Coercivity is often enhanced in $Nd_2Fe_{14}B$ by the addition of dysprosium. There are commercially available sintered $Nd_2Fe_{14}B$ magnets with a coercivity of $\sim 3,000$ kA/m (~ 38 kOe). Shorter specimens are more susceptible to internal demagnetization and, therefore, must have higher coercivity to match application specific requirements. AlNiCo magnets typically have low coercivity and, thus, must be made long and thin in order to minimize any demagnetization effect. One can select an optimized geometry by using the load lines and/or permeance coefficients of permanent magnets, as shown in **Figure 2**.⁴

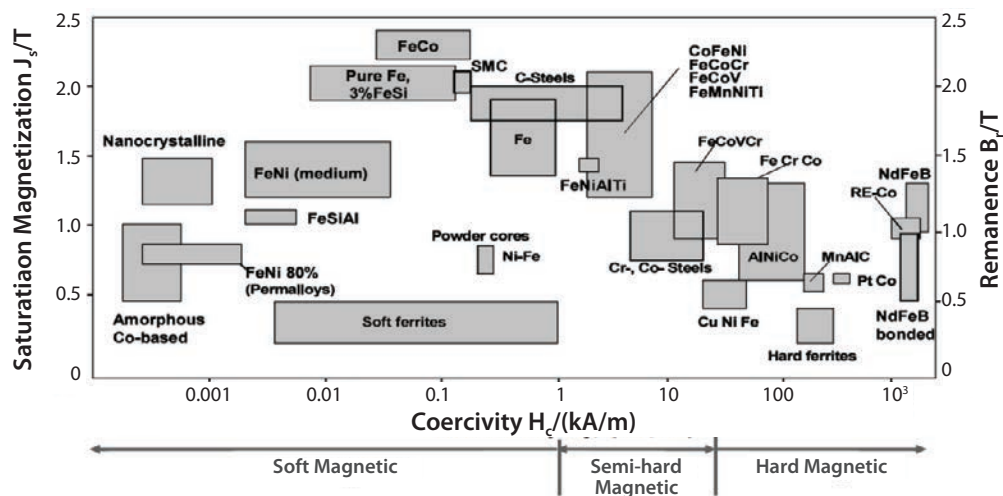


Figure 1. Coercivity, saturation magnetization, and remanence of various magnetic materials.³

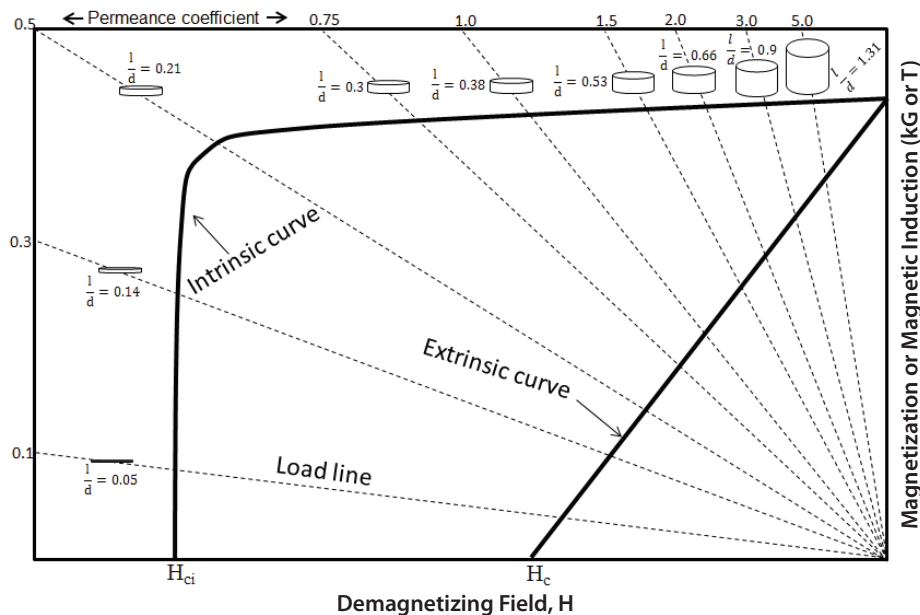


Figure 2. Demagnetization curve of a sintered $\text{Nd}_2\text{Fe}_{14}\text{B}$ magnet showing the permeance coefficient and corresponding sample geometries for each load line.

Remanence

Remanence is the residual magnetization that remains when no magnetic field is applied to a magnetic material that was previously magnetized to saturation. It is often used interchangeably with the term remanent magnetization, or the residual magnetization when no magnetic field is applied, whether or not the material was previously magnetized to saturation. Remanence is directly related to the amount of magnetic flux that can be generated with a permanent magnet. Figure 1 also shows the remanence values of different magnetic materials. Soft magnetic Fe–Co alloys have significantly higher remanence than permanent magnet materials. In permanent magnets, remanence values obtained with closed loop measurement systems will be higher than the open loop remanent magnetization since the effective field under closed loop configurations is identical with the applied field. This means that in applications that are normally open loop conditions, the remanent magnetization under which a permanent magnet operates will be less than its remanence value. In specimens with very low demagnetizing factors (e.g., toroid and long cylinders), the remanence in open loop configurations approaches that of closed loop configurations. However, as specimens become shorter and thicker, the opposite is true. This is important in selecting the geometry of permanent magnets for applications.

Maximum Energy Product

The *maximum energy product*, BH_{max} , has gained wide acceptance as a property to qualify the performance of permanent magnets. It is the maximum value of the product BH obtained in the second quadrant of the demagnetization plot and represents the maximum energy a permanent magnet can generate outside the magnet,¹ measured in MGOe (cgs) or kJ/m^3 (S.I.). The significance of BH_{max} in designing permanent magnet machines can be appreciated considering that the energy produced by a magnet of fixed size in an air gap outside the magnet is proportional to the product BH . As a result, the volume of magnet required to generate a given magnetic field strength outside the magnet is minimized when the product of BH is at the maximum value.⁵ Therefore in spatially restricted applications where smaller magnets are required, permanent magnets with a higher BH_{max} value can be used to maximize performance. Considering BH_{max} alone may not be sufficient to select a material for an application because it does not reflect the

demagnetizing effect imposed by the shape of the permanent magnet. In applications where spatial constraints require a shorter and thicker magnet, the magnet should be operated close to the maximum coercivity in order to minimize the effect of the demagnetizing field, even when it does not coincide with the point where the product BH is at the maximum. Ceramic magnets (ferrites) have low BH_{max} values but due to their higher coercivity may be preferred to AlNiCo magnets for such applications. Conversely, if a large magnetic flux is more important than resistance to demagnetization, long specimens of AlNiCo magnets are preferred to ceramic magnets in order to operate at the highest value of BH where the high remanence in AlNiCo can be utilized. In general, to maximize the energy generated from a permanent magnet in a given application, one needs to select a load line that maximizes the product BH while also meeting geometrical requirements. The room temperature demagnetization plot of a sintered $\text{Nd}_2\text{Fe}_{14}\text{B}$ magnet in Figure 2 shows the permeance coefficient and the corresponding sample geometries for each load line. The operating point of the magnet is the intersection between the load line and the extrinsic magnetization curve.

Magnetic Anisotropy

The term *magnetic anisotropy* refers to the directional dependence of magnetic properties. Magnetocrystalline anisotropy, significantly exploited in developing permanent magnets, is an intrinsic form of magnetic anisotropy. The consequence of magnetocrystalline anisotropy is that materials are easier to magnetize in certain crystallographic directions than in others. The energy that aligns the magnetic moments in the easy magnetization direction is the magnetocrystalline anisotropy energy. It arises from the coupling between the spin and orbital motions of electrons (spin-orbit coupling) and, therefore, may be considered as the energy required to overcome the spin-orbit coupling.⁶ It is often expressed in terms of the magnetocrystalline anisotropy constant, K_1 (ignoring the higher order constants; K_2, K_3, \dots , which may be significant in certain conditions). If K_1 is positive, there is an easy axis and a hard plane. If K_1 is negative, there is a hard axis and an easy plane. Materials with low crystal symmetry typically have higher anisotropy constants than those with higher symmetry. For example the magnetocrystalline anisotropy in hexagonal cobalt is an order of magnitude higher than that in iron with a cubic crystal structure. The relatively high anisotropy

of CoFe_2O_4 compared to other cubic materials is due to the contribution of the unquenched orbital angular momentum of Co to spin-orbit coupling.⁷ The contribution to the spin-orbit coupling that results in high magnetocrystalline anisotropy in rare-earth based permanent magnets comes from the rare-earth $4f$ electrons. The rotation of the magnetic moments in response to an applied magnetic field can be viewed as the competition between the magnetic energy and the magnetocrystalline anisotropy energy. The magnetic field strength required to rotate magnetic moments, inclined at an angle θ to the field direction, into the field direction is given in **Equation 1**. When the magnetic moments lie along the easy direction at 90° to the field direction, the magnetic field strength (H) needed to rotate magnetization into the field direction is the equivalent of the anisotropy field (H_A) given in **Equation 2**. To attain saturation magnetization, magnetic field strength equal to or greater than the anisotropy field needs to be applied.

$$H = \frac{2K_1 \sin \Theta}{M} \quad (1)$$

$$H_A = \frac{2K_1}{M_s} \quad (2)$$

Equation 2 is important for developing permanent magnets and shows why high magnetocrystalline anisotropy is desirable. The anisotropy field is often considered the maximum attainable coercivity in permanent magnets for a material magnetized to saturation. Applying this to permanent magnet manufacturing requires that the easy magnetization directions in all the grains constituting a permanent magnet be aligned. Once aligned, a strong magnetic field is required to rotate them and, thus, they are not easily demagnetized. This helps to relate magnetocrystalline anisotropy (an intrinsic property) to coercivity (a measure of resistance to demagnetization) which is an extrinsic magnetic property. It also shows why magnetocrystalline anisotropy is one qualifying criteria for selecting materials in permanent magnet applications. So far, the discussion on anisotropy assumes that the magnet acts as a uniformly magnetized piece in which all magnetic moments rotate uniformly when a magnetic field is applied. In practice, there are regions of uniform magnetization called magnetic domains, separated by domain walls—regions in which magnetization gradually switches from the direction in a domain to that in an adjacent domain.⁸ There is, therefore, another energy that competes with the magnetocrystalline anisotropy energy called the exchange energy. Exchange energy tends to increase the thickness of the domain walls, whereas anisotropy energy tends to decrease it. In addition, microstructural imperfections that obstruct the propagation of magnetic domains also contribute to coercivity. In practice, measured coercivity is less than the anisotropy field demonstrating that coercivity in an extrinsic property which, apart from anisotropy, depends on other factors.⁹

Shape Anisotropy

Shape anisotropy can also be crucial in permanent magnet development and applications. Due to shape anisotropy, it is easier to magnetize a material along the longer axis in which the demagnetizing field is less, than along the shorter axis which has a stronger demagnetizing effect. Since an applied magnetic field must overcome the anisotropy field, in addition to rotating the magnetic moments, the effective field (H_{eff}) is smaller than the applied field (H_{app}) by the magnitude of the demagnetizing field ($H_d = N_d M$), as shown in **Equation 3**. The demagnetizing field depends on the geometry of the material (represented by the demagnetization factor, N_d) and the magnetization in the material.

$$H_{\text{eff}} = H_{\text{app}} - N_d M \quad (3)$$

In producing AlNiCo magnets, efforts are focused toward enhancing shape anisotropy because the coercivity in AlNiCo is derived mainly from that shape anisotropy. In permanent magnet machine designs, the effect of shape anisotropy is also accommodated by selecting the appropriate load lines.

Curie Temperature

Ferromagnets (and ferrimagnets) transition to a paramagnetic state above their *Curie temperature*: a structure-insensitive magnetic property of materials. Above the Curie temperature, thermal energy overcomes the interaction energy that keeps the magnetic moments aligned, resulting in disordered magnetic moments, a sudden drop in magnetic susceptibility, zero remanence, and zero coercivity. High Curie temperatures are, therefore, desirable in order to use permanent magnets at elevated temperatures. Since magnetic properties continuously degrade as specimen temperature approaches the Curie temperature, there is typically a temperature (below the Curie temperature) above which a permanent magnet will perform below its rating. This temperature is called the maximum operating temperature or maximum working temperature. Typical $\text{Nd}_2\text{Fe}_{14}\text{B}$ magnets have Curie temperatures in the range $300\text{--}320^\circ\text{C}$, but the maximum operating temperatures are often between $80\text{--}120^\circ\text{C}$. Ultra-high grade $\text{Nd}_2\text{Fe}_{14}\text{B}$ magnets have a maximum operating temperature of $\sim 180^\circ\text{C}$.

Two other parameters are also important for describing the temperature dependence of the properties of permanent magnets. The reversible temperature coefficient of residual magnetic induction (α) is the percentage change in magnetic induction with change in temperature. Similarly, the reversible temperature coefficient of coercivity (β) is the percentage change in coercivity with temperature change. Depending on the application, these parameters can play a key role in the choice of a permanent magnet material. For example, permanent magnets used in applications like gyroscopes and accelerometers should have as low an α value as possible.¹⁰

Apart from the properties discussed so far, there are other aspects that can influence the choice of one permanent magnet material over another in an application. One example is corrosion resistance. Sintered NdFeB magnets are known to be very susceptible to corrosion due to multiple microstructural phases and can corrode faster than iron.⁵ Hence, these materials are usually coated with nickel, zinc, and aluminum. In polymer-bonded magnets, the binder material provides protection from corrosion. One advantage of samarium cobalt magnets is that they are less susceptible to corrosion than NdFeB magnets. Nevertheless, NdFeB magnets have better tensile, bending, and compressive strengths. As a result, Sm-Co magnets are more prone to breakage than NdFeB magnets. Ferrites and AlNiCo-based magnets have much better corrosion resistance than the rare-earth based magnets, but ferrite magnets are more brittle than AlNiCo magnets.

Additive Manufacturing

During the last decade, the use of permanent magnets in green energy technologies has skyrocketed. Rare-earth based permanent magnets such as $\text{Nd}_2\text{Fe}_{14}\text{B}$ (NdFeB) and SmCo_5 are essential components in mass market products such as audio speakers, hard-disk drives, elevators, electric vehicles, wind turbines, and aerospace applications. However, the high cost of rare-earth magnets, supply and availability of rare-earth resources, and the technical issues associated with the reliability of clean technology devices needs to be resolved in the future. The high cost of permanent magnets is mainly a result of the uncertainties of rare-earth elements. Considering that most of the US rare-earth magnet manufacturing capability was transferred to Asia and Europe in the last decade,¹¹ novel methods that avoid or minimize the use of rare-earth elements need to

be developed to reduce US vulnerability to rare-earth price spikes. One of the main strategies of the Critical Materials Institute research is to develop a viable additive manufacturing technique for the fabrication of near-net shape magnets. Conventional manufacturing methods used to make permanent magnets are inefficient and generate a sizeable waste during cutting and slicing of magnets to the required shapes and sizes. Recovering and remanufacturing rare-earth elements from the waste material is also not an easy task considering that rare-earth elements tend to oxidize. Therefore, alternative methods are needed that not only require less energy during manufacturing but also generate less waste material. One way to minimize the waste generated during permanent magnet manufacturing, and to reduce its overall cost, is to use additive methods to fabricate complex geometries of magnets that minimize waste. The additive manufacturing approach has the additional advantage of enabling the fabrication of physical parts directly from the computer-aided design (CAD) models, with no tooling required for fabricating magnets. In addition, the microstructure and properties of the magnets can be tailored using some additive manufacturing processes. Fabrication of magnets with metal additive manufacturing processes such as electron beam melting, laser additive manufacturing, electrophoretic deposition, and cold-spray deposition techniques are currently in development and testing, with results expected in the near future. Unlike conventional techniques, metal and polymer additive techniques make highly efficient use of energy and raw materials because materials are deposited only where they are needed. At the same time, additive manufacturing eliminates the need for specialized tools to make certain shapes and sizes.

Bonded NdFeB permanent magnets have grown into an important segment of the permanent magnet market with an estimated global market size of over \$750 million. Bonded magnet manufacturing processes include: compaction (using thermoset polymers such as epoxy, acrylic, phenolic, etc. and a curing temperature of 150–175 °C); injection (using thermoplastic polymers such as nylon, polyphenylene sulfide (PPS), etc.); elastomers (using nitrile rubber, vinyl, etc.); and calendaring process.^{12–20} Two manufacturing methods are typically utilized to fabricate the majority of bonded Neo magnets including injection molding using a thermoplastic binder and compression bonding using a thermoset binder. The reported energy product for injection-molded bonded Neo magnets ranges between 5–11 MGOe. However, for compaction bonded Neo magnets, a relatively higher energy product of 8–17 MGOe has been achieved. Bonded NdFeB magnets have better corrosion resistance and better ductile properties compared to sintered NdFeB magnets. Recently, isotropic NdFeB-bonded magnets with complex shapes have been successfully printed using direct write methods,²¹ binderjet printing,²² and big area additive manufacturing²³ techniques. The challenge in additive printing of anisotropic NdFeB magnets is increasing the magnet loading of >65 vol% while still maintaining anisotropy with perfect grain alignment in complex shapes and throughout the thickness of the magnet. Thus, innovative methods are still needed to produce NdFeB-bonded magnets with high energy products.

Exploiting the Mesoscale with Exchange Spring Magnets (A New Type of Hybrid)

Nanocomposite exchange spring permanent magnets are one composition with the potential to exceed the performance of current state-of-the-art sintered rare-earth permanent magnets.²⁴ The potential of exchange spring magnets comes from their remanent magnetization enhanced by a highly magnetized soft phase such as iron, while exhibiting high intrinsic coercivity at the same time. This high intrinsic coercivity is provided by a hard magnet phase with large, uniaxial magnetocrystalline anisotropy. Early work predicted energy products as high as 120 MGOe (1 MJ/m³).²⁵ More recent numerical simulations have suggested that energy products of 85.2 MGOe (0.678 MJ/m³) may be

more attainable.²⁶ This value is still in excess of the maximum possible energy product of 64 MGOe (0.515 MJ/m³) exhibited by Nd₂Fe₁₄B sintered permanent magnets.²⁷ Such a property improvement in nanocomposite magnets requires three conditions be met: (1) the saturation magnetization of the soft phase must exceed that of the hard phase; (2) the magnetically “easy” axes of the hard phase components must be aligned parallel to one another; and (3) the characteristic dimensions of the microstructure (for example, grain size) must be fine enough to allow the phases to be magnetically coupled by the ferromagnetic exchange interaction. **Figure 3** is a schematic of the microstructure of a conceptual nanocomposite magnet.

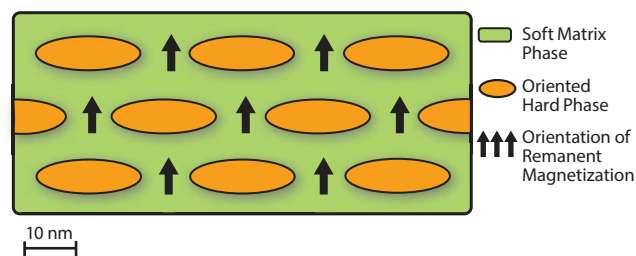


Figure 3. Schematic of nanocomposite magnet microstructure illustrating the key requirements of particle size and orientation.

To date, these three requirements have been fully met only in composites produced by thin and/or thick film processing methods.^{28–31} Isotropic nanocomposite magnets have been produced by rapidly solidifying Nd₂Fe₁₄B alloyed with an excess of Fe.³² Under certain rapid quenching and annealing conditions, these magnets may form a two-phase structure that contains nanometer-sized grains of α -Fe and Nd₂Fe₁₄B.³³ The magnetic remanence (B_r) is enhanced when compared to an isotropic magnet produced without excess Fe. However, this “top-down” processing method does not enable easy axis alignment of the Nd₂Fe₁₄B. Thus, the energy products of these magnets are lower than those manufactured by high temperature sintering of magnetically aligned powders. Isotropic nanocomposite magnets have been commercialized in bulk as polymer-bonded magnets by Magnequench.

The development of bulk nanocomposite magnets also includes “bottom-up” processing methods in which hard and soft magnetic phases are first produced as discrete nanoparticles that are then aligned and consolidated into bulk shapes. This route requires selection and development of multiple processing methods. Particle processing methods have included chemical, electrochemical, mechanical, and plasma synthesis methods.^{34,35} Both magnetic and mechanical particle alignment methods have been explored. Consolidation methods have included conventional thermal sintering as well as shear-assisted methods such as uniaxial and triaxial compaction, extreme shear deformation methods, and specialized methods such as spark-plasma sintering and dynamic magnetic compaction.^{36,37}

Among the many challenges facing the various bottom-up processing methods is the need to retain the nanometer-scale dimensions of the discrete nanoparticles during consolidation and alignment. The large driving force for minimization of surface energy due to thermally activated particle coarsening makes conventional high temperature sintering processes impractical. Large surface area-to-volume ratios combined with the use of reactive rare-earth compounds make the nanoparticle precursor compounds extremely air sensitive and necessitate the use of inert-atmosphere environments with strict oxygen control. The hard and soft magnetic phases used in nanocomposite permanent magnets may not be thermodynamically stable in combination, leading to a metastable structure. Computational methods enable the prediction of magnetization curves and reversal fields for idealized nanocomposite microstructures.^{38–41} Both hard phase particles embedded in a soft phase matrix and hard phase particles embedded in a soft phase matrix have been numerically

simulated. The calculations have progressed to the point where preferred microstructural dimensions can be specified for composite structures with regular structures and connectivity patterns. Additionally, progress has been made in understanding the dependence of coercivity on soft phase content. Further work must be performed to simulate irregular microstructures that are produced in practice, as well as to better understand the influence of temperature on composite magnetic properties. Experimental⁴² and computational⁴³ work has also explored the fundamental nature of the magnetic coupling that exists at the interface between the hard and soft phases in nanocomposite magnets. Less work has been performed in bulk nanocomposite magnets. It is likely that advanced three-dimensional atom probe methods would be well-suited to characterization of the fine structure of nanocomposite magnets. Substantial progress has been made over the past 25 years toward achieving the goal of higher energy product nanocomposite permanent magnets. This progress has been paced by concurrent advances in materials processing, characterization, and simulation technology. The need for high efficiency, environmentally sustainable electric power and transportation systems remains a key priority. This need justifies continued investment in novel permanent magnet materials.

Acknowledgment

This work was supported by the Critical Materials Institute, an Energy Innovation Hub funded by the U.S. Department of Energy, Office of Energy Efficiency and Renewable Energy, Advanced Manufacturing Office. Work at Ames Laboratory, operated by Iowa State University, was performed under Contract No. DE-AC02-07CH11358. Partially prepared by LLNL under Contract DE-AC52-07NA27344.

Notice: This manuscript has been authored by UT-Battelle, LLC under Contract No. DE-AC05-00OR22725 with the U.S. Department of Energy. The United States Government retains and the publisher, by accepting the article for publication, acknowledges that the United States Government retains a non-exclusive, paid-up, irrevocable, world-wide license to publish or reproduce the published form of this manuscript, or allow others to do so, for United States Government purposes. The Department of Energy will provide public access to these results of federally sponsored research in accordance with the DOE Public Access Plan (<http://energy.gov/downloads/doe-public-access-plan>).

References

- Jiles, D. *Introduction to Magnetism and Magnetic Materials*, 2nd ed., Chapman and Hall, New York, **1998**.
- Bozorth, R. M. *Ferromagnetism*, D. Van Nostrand Company, Inc., New York, **1951**.
- Weickhmann, M. *NdFeB Magnets Properties and Applications*, **2009**, 1–10.
- Gutfleisch, O.; Willard, M. A.; Brück, E.; Chen, C. H.; Sankar, S. G.; Liu, J. P. *Adv. Mater.* **2011**, *23*, 821–42.
- Coey, J. M. D. *Rare-earth Iron Permanent Magnets*, Clarendon Press, Oxford, **1996**.
- Spaldin, N. A. *Magnetic Materials: Fundamentals and Applications*, 2nd ed., Cambridge University Press, New York, **2011**.
- Nlebedim, I. C.; Snyder, J. E.; Moses, A. J.; Jiles, D. C. *IEEE Trans. Magn.* **2012**, *48*, 3084–3087.
- Buschow, K. H.; de Boer, F. R. *Physics of Magnetism and Magnetic Materials*, 1st ed., Kluwer Academic Publishers-Plenum Publishers, New York, **2003**.
- Givord, D.; Rossignol, M. F.; Taylor, D. W., Jr. *Phys. Rev. B* **1972**, *6*, 3–95–C3–104.
- Martis, R.; Gupta, N.; Sankar, S.; Rao, V. *IEEE Trans. Magn.* **1978**, *15*, 948–950.
- Lewis, L. H.; Jimenez-Villacorta, F. *Metall. Trans. A* **2013**, *4*, 52.
- Ormerod, J.; Constantinides, S. *J. Appl. Phys.* **1997**, *81*, 4816–4820.
- Hamada, N.; Mishima, C.; Mitarai, H.; Honkura, Y. *IEEE Trans. Magn.* **2003**, *39*, 2953–2955.
- Hamada, N.; Noguchi, K.; Mishima, C.; Honkura, Y. *Digests of the IEEE International Conference*. **2005**, 941–942 (2005). DOI: 10.1109/INTMAG.2005.1463899.
- Croat, J. J. *J. Appl. Phys.* **1997**, *81*, 4804–4809.
- Sugimoto, S. *J. Phys. D: Appl. Phys.* **2011**, *44*, 064001.
- Brown, D.; Ma, B.-M.; Chen, Z. *J. Mag. Mat.* **2002**, *248*, 432.
- Brown, D. N.; Wu, Z.; He, F.; Miller, D. J.; Herchenroeder, J. W. *J. Phys. Cond. Mat.* **2014**, *26*, 064202.
- Hamada, N.; Noguchi, K.; Mishima, C.; Honkura, Y. *IEEE Trans. Magn.* **2005**, *41*, 3847–3829.
- Brown, D. N.; Chen, Z.; Guschl, P.; Campbell, P. *J. Mag. Mat.* **2006**, *303*, 371–374.
- Compton, B. G.; Kemp, J. W.; Novikov, T. V.; Pack, R. C.; Nlebedim, I. C.; Duty, C. E.; Rios, O.; Paranthaman, M. P. *Mater. Manuf. Process.* **2016**, doi.org/10.1080/10426914.2016.1221097.
- Paranthaman, M. P.; Shafer, C. S.; Elliott, A. M.; Siddel, D. H.; McGuire, M. A.; Springfield, R. M.; Martin, J.; Fredette, R.; Ormerod, J. *JOM* **2016**, *68*, 1978.
- Li, L.; Tirado, A.; Nlebedim, I. C.; Rios, O.; Post, B.; Kunc, V.; Lowden, R. R.; Lara-Curzio, E.; Fredette, R.; Ormerod, J.; Lograsso, T. A.; Paranthaman, M. P. *Scientific Reports* **2016**, *6*, doi:10.1038/srep36212.
- Kneller, E. F.; Hawig, R. *IEEE Trans. Mag.* **1991**, *27*, 3588.
- Skomski, R.; Coey, J. M. D. *Phys. Rev. B* **1993**, *48*, 15812.
- Jiang, J. S. *J. of Phys.: Condensed Mat.* **2014**, *26*, 064214.
- Herbst, J. F. *Rev. Mod. Phys.* **1991**, *63*, 819.
- Fullerton, E. E.; Jiang, J. S.; Grimsditch, M.; Sowers, C. H.; Bader, S. D. *Phys. Rev. B* **1998**, *58*, 12193.
- Zhang, J.; Takahashi, Y. K.; Gopalan, R.; Hono, K. *Appl. Phys. Lett.* **2005**, *86*, 122509.
- Liu, Y.; Wu, Y. Q.; Kramer, M. J.; Choi, Y.; Jiang, J. S.; Wang, Z. L.; Liu, J. P. *Appl. Phys. Lett.* **2008**, *93*, 192502.
- Fukunaga, H.; Tou, A.; Itakura, M.; Nakano, M.; Yanai, T. *IEEE Trans. Mag.* **2014**, *50*, 2101504.
- Hirosawa, S.; Kanekiyo, H.; Miyoshi, T. *J. Mag. Mat.* **2004**, *281*, 58.
- Chen, Z.; Brown, D. N.; Ma, B. M.; Campbell, P.; Wu, Y. Q.; Kramer, M. J. *IEEE Trans. Mag.* **2005**, *41*, 3862.
- Willard, M. A.; Kurihara, L. K.; Carpenter, E. E.; Calvin, S.; Harris, V. G. *Int. Mater. Rev.* **2004**, *49*, 125.
- Frey, N. A.; Peng, S.; Cheng, K.; Sun, S. *Chem. Soc. Rev.* **2009**, *38*, 2532.
- Poudyal, N.; Liu, J. P. *J. Phys. D* **2013**, *46*, 043001.
- Balamurugan, B.; Sellmyer, D. J.; Hadjipanayis, G. C.; Skomski, R. *Scripta Mat.* **2012**, *67*, 542.
- Schrefl, T.; Fidler, J.; Kronmüller, H. *Phys. Rev. B* **1994**, *49*, 6100.
- Fidler, J.; Schrefl, T. *J. Phys. D: Appl. Phys.* **2000**, *33*, R135.
- Fukunaga, H.; Horikawa, R.; Nakano, M.; Yanai, T.; Fukuzaki, T.; Abe, K. *IEEE Trans. Mag.* **2013**, *49*, 3240.
- Skomski, R.; Manchanda, P.; Kumar, P.; Balamurugan, B.; Kashyap, A.; Sellmyer, D. J. *IEEE Trans. Mag.* **2013**, *49*, 3215.
- Choi, Y.; Jiang, J. S.; Ding, Y.; Rosenberg, R. A.; Pearson, J. E.; Bader, S. D.; Zambano, A.; Murakami, M.; Takeuchi, I.; Wang, Z. L.; Liu, J. P. *Phys. Rev. B* **2007**, *75*, 104432.
- Fukunaga, H.; Mukaino, H. *J. Rare Earths*. **2004**, *22*, 146.

Metallic Powders

For a complete list of available materials, visit aldrich.com/metals.

Name	Purity	Resistivity ($\mu\Omega\text{-cm}$)	Avg. Part. Size	Prod. No.
Aluminum, Al	$\geq 99.95\%$ trace metals basis	resistivity 2.6548	<75 μm	202584-10G
Antimony, Sb	99.5% trace metals basis	resistance 41.7	-100 mesh	266329-250G 266329-1KG
Bismuth, Bi	$\geq 99.99\%$ trace metals basis	resistivity 129 (20 °C)	-100 mesh	264008-25G
	99% trace metals basis	resistivity 129 (20 °C)	-100 mesh	265462-100G 265462-500G
Cerium, Ce	99.9% trace rare earth metals basis	resistivity 73 (20 °C)	-40 mesh	263001-10G
Cobalt, Co	$\geq 99.9\%$ trace metals basis	resistivity 6.24 (20 °C)	<150 μm	266647-50G 266647-250G
Copper, Cu	99.999% trace metals basis	resistivity 1.673 (20 °C)	-	203122-10G 203122-50G
	99%	resistivity 1.673 (20 °C)	<75 μm	207780-500G 207780-2KG
	99%	resistivity 1.673 (20 °C)	14 – 25 μm	326453-250G 326453-1KG
	99.7% trace metals basis	resistivity 1.673 (20 °C)	<45 μm	357456-100G 357456-500G
Erbium, Er	99.9% trace rare earth metals basis	resistivity 86 (20 °C)	-40 mesh	263044-5G
Germanium, Ge	$\geq 99.999\%$ trace metals basis	resistivity 53000 (20 °C)	-100 mesh	327395-5G 327395-25G
	$\geq 99.99\%$ trace metals basis	resistivity 53000 (20 °C)	-100 mesh	203351-10G 203351-50G
Hafnium, Hf	99.5% trace metals basis (purity excludes ~2% zirconium)	resistivity 29.6 (0 °C)	-325 mesh	266752-25G
Indium, In	99.999% trace metals basis	resistivity 8.37	-60 mesh	203432-5G 203432-25G
	99.99% trace metals basis	resistivity 8.37	-100 mesh	264032-5G 264032-25G
	99.99% trace metals basis (Purity excludes ~1% Mg as anticaking agent)	resistivity 8.37	-	277959-10G 277959-50G
Lanthanum, La	99.9% trace rare earth metals basis	resistivity 54	-40 mesh	263109-25G
Lead, Pb	99.95% trace metals basis	resistivity 20.65	-100 mesh	391352-100G
	$\geq 99\%$ trace metals basis	resistivity 20.65	-325 mesh	209708-1KG 209708-5KG
Manganese, Mn	$\geq 99\%$ trace metals basis	resistivity 185 (20 °C)	-325 mesh	266132-250G 266132-1KG
	$\geq 99.9\%$ trace metals basis	resistivity 185 (20 °C)	-	463728-25G 463728-100G
Molybdenum, Mo	99.99% trace metals basis	resistivity 5.0 (20 °C)	<150 μm	203823-100G
	99.9% trace metals basis	resistivity 5.0 (20 °C)	<150 μm	266892-100G
	$\geq 99.95\%$ trace metals basis	resistivity 5.0 (20 °C)	10 μm	366986-10G
	$\geq 99.9\%$ trace metals basis	resistivity 5.0 (20 °C)	1–5 μm	510092-50G 510092-250G
Neodymium, Nd	$\geq 99\%$ trace rare earth metals basis	resistivity 64.0 (20 °C)	-40 mesh	460877-10G
Nickel, Ni	99.99% trace metals basis	resistivity 6.97 (20 °C)	<150 μm	203904-25G 203904-100G 203904-500G
	99.7% trace metals basis	resistivity 6.97 (20 °C)	<50 μm	266981-100G 266981-500G
	99.8% trace metals basis	resistivity 6.97 (20 °C)	<1 μm	268283-25G
Palladium, Pd	99.999% trace metals basis	resistivity 9.96 (20 °C)	0.25–2.36 mm	203939-1G 203939-5G
	99.9% trace metals basis	resistivity 9.96 (20 °C)	<75 μm	464651-5G
	$\geq 99.9\%$ trace metals basis	resistivity 9.96 (20 °C)	<1 μm	326666-1G 326666-5G
Platinum, Pt	99.995% trace metals basis	resistivity 10.6 (20 °C)	-	204013-1G
Praseodymium, Pr	99.5% trace rare earth metals basis	resistivity 68 (20 °C)	~40 mesh	263176-5G

Name	Purity	Resistivity ($\mu\Omega\text{-cm}$)	Avg. Part. Size	Prod. No.
Rhodium, Rh	99.95% trace metals basis	resistivity 4.33 (20 °C)	-	204218-1G
Ruthenium, Ru	99.99% trace metals basis	resistivity 7.1 (0 °C)	-	545023-1G
	99.9% trace metals basis	resistivity 7.1 (0 °C)	-200 mesh	209694-5G
Scandium, Sc	99.9% trace rare earth metals basis	resistivity 50.5 (0 °C)	-	261262-250MG 261262-1G
Silicon, Si	99.999% trace metals basis	-	-60 mesh	267414-25G
	99% trace metals basis	-	-325 mesh	215619-50G 215619-250G 215619-1KG
Silver, Ag	99.99% trace metals basis	resistivity 1.59 (20 °C)	<250 μm	265500-10G
	$\geq 99.99\%$ trace metals basis	resistivity 1.59 (20 °C)	<45 μm	327107-10G 327107-50G
	$\geq 99.9\%$ trace metals basis	resistivity 1.59 (20 °C)	5–8 μm	327093-10G 327093-50G
	$\geq 99.9\%$ trace metals basis	resistivity 1.59 (20 °C)	2–3.5 μm	327085-10G 327085-50G
Tantalum, Ta	99.99% trace metals basis	resistivity 13.5 (20 °C)	-	545007-10G
	99.9%	resistivity 13.5 (20 °C)	60 – 100 mesh	692824-5G
	99.9% trace metals basis	resistivity 13.5 (20 °C)	-325 mesh	262846-25G 262846-100G
Tin, Sn	99.99% trace metals basis	resistivity 11 (20 °C)	-100 mesh	755702-5G
Titanium, Ti	99.7% trace metals basis	resistivity 42.0 (20 °C)	-100 mesh	268496-50G
	99.98% trace metals basis	resistivity 42.0 (20 °C)	<45 μm	366994-10G 366994-50G
Tungsten, W	99.9% trace metals basis	resistivity 4.9 (20 °C)	12 μm	267511-100G 267511-500G
	$\geq 99.99\%$ trace metals basis	resistivity 4.9 (20 °C)	10 μm	357421-10G
	$\geq 99.9\%$ trace metals basis	resistivity 4.9 (20 °C)	0.6–1 μm	510106-500G
Ytterbium, Yb	$\geq 99.9\%$ trace rare earth metals basis	resistivity 28 (20 °C)	-	466069-2G
Yttrium, Y	99.5% trace rare earth metals basis	resistivity 57 (20 °C)	-40 mesh	261327-5G 261327-25G
Zinc, Zn	99.995% trace metals basis	resistivity 5.8 (20 °C)	<150 μm	324930-10G 324930-50G
Zirconium, Zr	-	resistivity 40 (20 °C)	-100 mesh	403296-50G
	99.5% trace metals basis (excluding Hf)	resistivity 40 (20 °C)	-325 mesh	756385-5G

3D Printable Graphene Ink

For a complete list of available materials, visit aldrich.com/3dp.

Particle Size (nm)	Viscosity (Pa.s)	Resistivity ($\Omega\text{-cm}$)	Prod. No.
1–15 (thick)	25–45 (At low shear stresses. Shear thins to ~10–15 Pa.s at Shear Stress = 100 Pa)	0.12–0.15 (as 3D-printed fibers, not ink, 200–400 μm diameter)	808156-5ML
1–20 (length and width)			

3D Printing Filaments

For a complete list of available materials, visit aldrich.com/3dp.

Carbon Fiber Reinforced Filaments

Weight = 750 g per spool

Description	Size (diam., mm)	Prod. No.
3DXMAX™ CFR-ABS carbon fiber reinforced ABS 3D printing filament	2.85	3DXCFR001-1EA
3DXMAX™ CFR-PLA carbon fiber reinforced PLA 3D printing filament	1.75	3DXCFR002-1EA
3DXMAX™ CFR-ABS carbon fiber reinforced ABS 3D printing filament	1.75	3DXCFR003-1EA
3DXMAX™ CFR-PLA carbon fiber reinforced PLA 3D printing filament	2.85	3DXCFR004-1EA

Carbon Nanotube Reinforced Filaments

Weight = 750 g per spool

Description	Size (diam., mm)	Prod. No.
3DXNANO™ ESD CNT-ABS carbon nanotube reinforced ABS 3D printing filament	1.75	3DXCNT001-1EA
3DXNANO™ ESD CNT-ABS carbon nanotube reinforced ABS 3D printing filament	2.85	3DXCNT002-1EA
3DXNANO™ ESD CNT-PETG carbon nanotube reinforced polyethylene terephthalate glycol copolymer 3D printing filament	1.75	3DXCNT003-1EA
3DXNANO™ ESD CNT-PETG carbon nanotube reinforced polyethylene terephthalate glycol copolymer 3D printing filament	2.85	3DXCNT004-1EA

Nylon/ABS Alloy

Weight = 500 g (1.1 lb)

Color	Size (diam., mm)	Prod. No.
black	1.75	3DXION001-1EA
blue	1.75	3DXION002-1EA
red	1.75	3DXION003-1EA
natural	1.75	3DXION004-1EA

ABS

Weight = 1 kg (2.2 lb) spool

Color	Size (diam., mm)	Prod. No.
black	1.75	3DXABS001-1EA
	2.85	3DXABS002-1EA
blue	1.75	3DXABS003-1EA
	2.85	3DXABS004-1EA
green	1.75	3DXABS005-1EA
	2.85	3DXABS006-1EA
natural	1.75	3DXABS007-1EA
	2.85	3DXABS008-1EA
orange	1.75	3DXABS009-1EA
	2.85	3DXABS010-1EA
red	1.75	3DXABS011-1EA
	2.85	3DXABS012-1EA
white	1.75	3DXABS013-1EA
	2.85	3DXABS014-1EA
yellow	1.75	3DXABS015-1EA
	2.85	3DXABS016-1EA

PLA

Weight = 1 kg (2.2 lb) spool

Color	Size (diam., mm)	Prod. No.
black	1.75	3DXPLA001-1EA
	2.85	3DXPLA002-1EA
blue	1.75	3DXPLA003-1EA
	2.85	3DXPLA004-1EA
green	1.75	3DXPLA005-1EA
	2.85	3DXPLA006-1EA
natural	1.75	3DXPLA007-1EA
	2.85	3DXPLA008-1EA
orange	1.75	3DXPLA009-1EA
	2.85	3DXPLA010-1EA
red	1.75	3DXPLA011-1EA
	2.85	3DXPLA012-1EA
white	1.75	3DXPLA013-1EA
	2.85	3DXPLA014-1EA
yellow	1.75	3DXPLA015-1EA
	2.85	3DXPLA016-1EA

CARBON NANOTUBE 3D PRINTING FILAMENTS

3DXNANO™ ESD Carbon Nanotube (CNT) Printing Filaments are used in critical applications that require electrostatic discharge (ESD) protection and a high level of cleanliness. The compounded filaments are formulated with premium Acrylonitrile Butadiene Styrene (ABS) or Polyethylene Terephthalate Glycol (PETG) resin and multi-walled CNTs in the presence of dispersion modifiers, resulting in a filament with excellent printing characteristics and consistent ESD properties.

Properties of 3DXNANO™ ESD 3D Printing Filaments

- Consistent surface resistivity (target $1.0 \times 10^7 - 10^9 \Omega$)
- Amorphous polymers – low and near isotropic shrinkage
- ABS suitable for water-based conformal coatings
- Low moisture absorption of PETG
- PETG preferred for solvent-based conformal coatings
- Excellent retention of base-resin ductility due to low loading rate of CNTs needed to achieve ESD
- Ultra-low particulate contamination vs. carbon black compounds



Name	Diameter (mm)	Prod. No.
3DXNANO™ ESD CNT-ABS 3D printing filament	1.75	3DXCNT001
	2.85	3DXCNT002
3DXNANO™ ESD CNT-PETG 3D printing filament	1.75	3DXCNT003
	2.85	3DXCNT004

For the complete nanomaterials offering, visit
[aldrich.com/3dp](https://www.aldrich.com/3dp)

RESPONSIVE RARE-EARTH MATERIALS AND THEIR APPLICATIONS



Yaroslav Mudryk
Ames Laboratory of U.S. Department of Energy,
Iowa State University
Ames, Iowa 50011 USA
Email: slavkomk@ameslab.gov

Introduction

The unique properties of the rare-earth elements and their alloys have brought them from relative obscurity to high profile use in common high-tech applications. The broad technological impact of these remarkable materials may have never been known by the general public if not for the supply concerns that placed the rare-earth materials on the front page of newspapers and magazines. Neodymium and dysprosium, two essential components of Nd₂Fe₁₄B-based high-performance permanent magnets, have drawn much attention and have been deemed critical materials for many energy-related applications. Ironically, the notoriety of rare-earth elements and their alloys is the result of a global movement to reduce their use in industrial applications and, thus, ease concerns about their supply and ultimately to reduce their position in high-tech supply chains.

Research into the applications of lanthanide alloys has been de-emphasized recently due to the perception that industry is moving away from the use of rare-earth elements in new products. While lanthanide supply challenges justify efforts to diversify the supply chain, a strategy to completely replace the materials overlooks the reasons rare earths became important in the first place—their unique properties are too beneficial to ignore. Rare-earth alloys and compounds possess truly exciting potential for basic science exploration and application development such as solid-state caloric cooling. In this brief review, we touch upon several promising systems containing lanthanide elements that show important and interesting magnetism-related phenomena. In particular, we will review several R₅T₄ (R = rare-earth element, T = 13–15th group p-element)¹ and RM₂ [M = either *p*- (e.g., Mg, Al) or *d*- (e.g., Fe, Ni, Co) metal]² compounds and their unusual responsiveness to external stimuli. Both systems are known to produce strong effects in response to applied magnetic fields and are sensitive to changes in composition, temperature, and pressure.

R₅T₄ Compounds—Unique Multifunctional Intermetallics for Basic Research and Applications

When a compound shows an extraordinarily strong response to a relatively weak external force, such as a moderately applied magnetic field, there is often significant potential for new fundamental science and technological applications. Systems such as R₅T₄, for example, can produce a drastic change in electrical transport or linear dimension in response to a relatively weak stimuli. The discovery of the giant magnetocaloric effect (GMCE) in Gd₅Si₂Ge₂ in 1997 by Pecharsky and Gschneidner^{3,4} immediately triggered a wave of both applied and fundamental research aimed at alloys with R₅(Si_xGe_{x'})₄ stoichiometry, or, in general, R₅T₄ compounds. Soon many other useful properties were found in these systems, including giant magnetoresistance (GMR),^{5,6} giant magnetostriction (GMS),⁷ and spontaneous generation of voltage (SGV),⁸ in addition to the observation of basic and very interesting phenomena, such as unconventional magnetic glass state,⁹ spin-flop transitions,¹⁰ magnetic deflagration,¹¹ and short-range magnetic correlations (Griffiths-like phase).¹² The fact that all these phenomena can occur simultaneously in the same material is interesting for fundamental research and shows a promising multifunctionality for use in applications. While most of these effects were originally discovered in Gd₅Si₂Ge₂ or similar compositions (e.g., Gd₅Si_{1.8}Ge_{2.2})^{6,7}, many other R₅T₄ systems also exhibit useful properties. For example, similar extraordinary responsive behavior is observed in compounds with a quasi-two-dimensional slab crystal structure such as orthorhombic Sm₅Ge₄- or monoclinic Gd₅Si₂Ge₂-types (Figure 1).

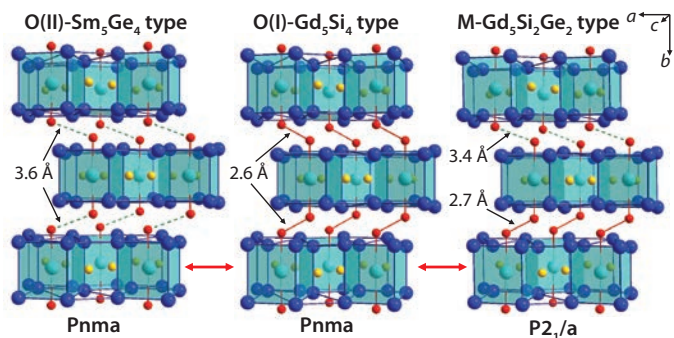


Figure 1. Schematic representation of the three main structure types, O(II)-Sm₅Ge₄, O(I)-Gd₅Si₄, and M-Gd₅Si₂Ge₂ commonly associated with magnetostructural transformations in R₅T₄ alloys. The slabs (shaded blue) do not change substantially during the transitions but the interslab T–T (interslab T atoms are marked red) bonds may break and re-form either fully or partially. In most cases, ferromagnetism occurs when both interslab T–T bonds are present (*d* = 2.6 Å, middle structure).

During magnetic transitions these slabs may shift with respect to each other, typically resulting in a structural transformation. As a result, another slab structure, orthorhombic Gd_5Si_4 , commonly forms when a material enters the ferromagnetic (FM) state. Consequently, the above mentioned physical effects are caused by the intimate coupling between magnetic and lattice states, and the transitions between the structures are followed by drastic changes in magnetization, lattice dimensions ($\Delta V/V$ up to 1.2%), lattice and magnetic entropy, electrical transport properties, and microstructure. The three main structure types involved in magnetostructural transformations in R_5T_4 systems are shown in Figure 1.

To describe the magnetostructural behavior in R_5T_4 , we'll use the $\text{Gd}_5\text{Si}_{0.5}\text{Ge}_{3.5}$ compound as an example.¹³ At room temperature, this material has the Sm_5Ge_4 -type structure and, when it orders antiferromagnetically at $T_N = 130$ K, there is no structural transformation. However, at T_c above 70 K, there is a sharp order-order antiferromagnetic/ferromagnetic transformation coupled with a Sm_5Ge_4 to Gd_5Si_4 structural transition (Figure 2). Due to such an abrupt and large change in magnetization, this alloy shows a giant magnetocaloric effect, $\Delta S_M = -44$ J/kg K, near the temperature of nitrogen liquefaction. In addition, as seen in Figure 2B, there is an unusually large and anisotropic change of lattice parameters at the transition since the upper limit for magnetostriction is above 18,000 ppm along the a -axis of the $\text{Gd}_5\text{Si}_{0.5}\text{Ge}_{3.5}$ crystal near liquid nitrogen temperature.

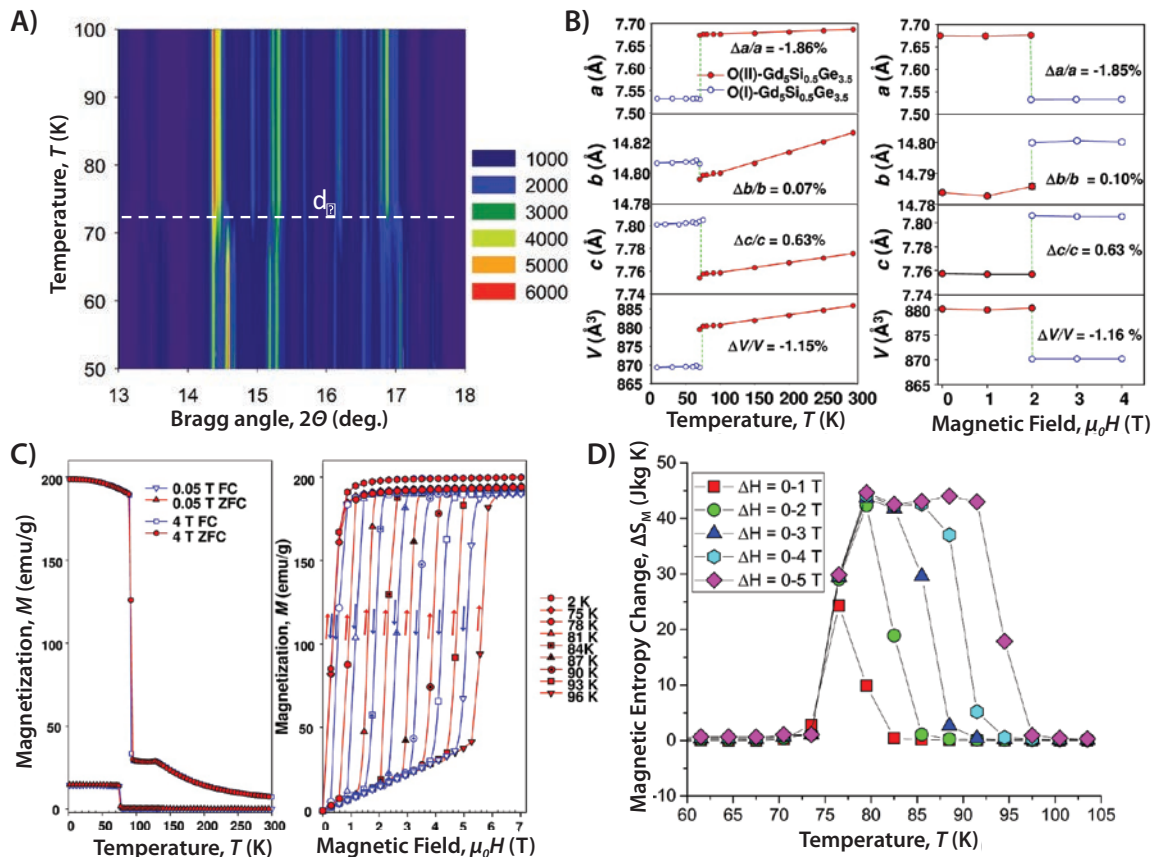


Figure 2. Magnetostructural transformation in $\text{Gd}_5\text{Si}_{0.5}\text{Ge}_{3.5}$: A) contour plot of the temperature-dependent X-ray powder diffraction patterns around the transition temperature T_c ; B) temperature (at 0 T) and magnetic-field (at 80 K) dependence of the lattice parameters and unit-cell volume; C) temperature and magnetic-field dependence of magnetization; and D) magnetocaloric effect (magnetic entropy change) as a function of temperature determined from the $M(H)$ data.¹³

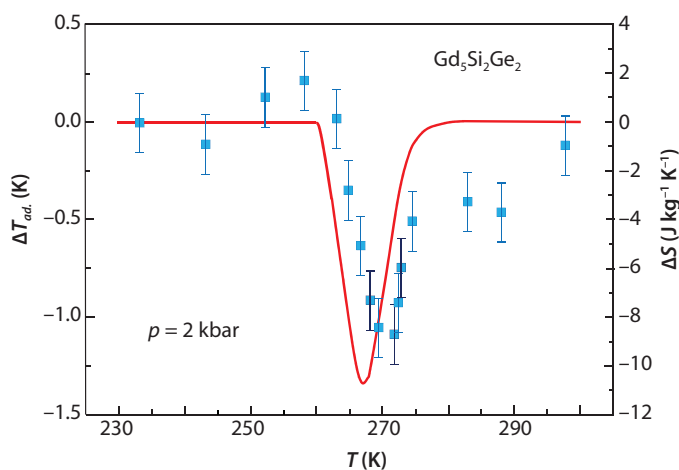


Figure 3. Barocaloric effect in $\text{Gd}_5\text{Si}_2\text{Ge}_2$; symbols show adiabatic temperature change corresponding to the release of pressure, $p = 2$ kbar. Solid line indicates isothermal entropy change corresponding to the release of pressure, $p = 2$ kbar.¹⁵

RM₂ Compounds – Simple Structures with Complex Physical Behavior

Intermetallic compounds with RM₂ stoichiometry crystallize at room temperature in the three closely related C14 hexagonal MgZn₂-type, C15 cubic MgCu₂-type, and C36 hexagonal MgNi₂-type structures.² They are commonly known as Laves phases and are one of the largest families of alloys in R-M systems. Many of the cubic RM₂ compounds undergo structural distortions at low temperatures, and these transitions are often coupled with magnetic ordering/reordering transformations. Depending upon the direction of the easy magnetization axis (EMA) below the transformation, RM₂ compounds with the room temperature cubic crystal structure may exhibit rhombohedral (for EMA <111>), tetragonal (EMA <100>), or orthorhombic (EMA <110>) distortions.^{16,17} Sometimes a compound may exhibit two structural transitions, first at the magnetic ordering temperature and then at the point of spin-reorientation (change of EMA). This has been observed, for example, in HoCo₂ (Figure 4).¹⁸

HoCo₂, as well as some other RM₂, has a first-order transition at T_C; but in the majority of RM₂ alloys the magnetic ordering transitions are second-order. The commonly shared understanding associates first-order behavior with the instability of transition metal moments. This instability means that even a small change to the external stimulus may lead to a sudden occurrence of magnetically ordered state which, as mentioned above, may result in a plethora of useful phenomena, such as the giant magnetocaloric effect, giant magnetoresistance, and giant magnetostriction. At the same time, the most famous magnetostrictive material, Terfenol-D (Tb_{0.7}Dy_{0.3}Fe₂), derives its properties from the strong anisotropic response (not first-order) of its lattice to applied magnetic field around room temperature. Unlike the abrupt response that occurs when a material undergoes a first-order transformation, the change of materials dimensions with field in Terfenol-D is gradual and can be precisely controlled. This fact illustrates the versatility of the RM₂ alloys, where both first- and second-order materials can find technological usefulness. The RM₂ alloys with M = Al, Co, and Ni are well-established candidates for low temperature magnetocaloric applications such as hydrogen liquefaction.

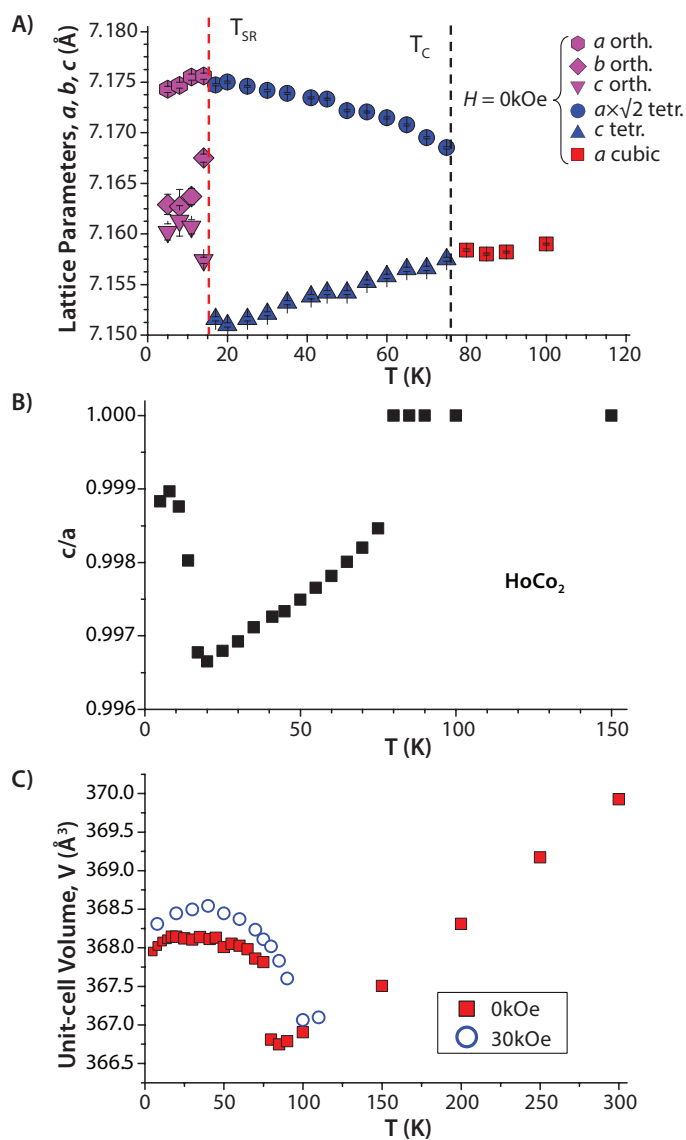


Figure 4. Magnetostructural transitions in HoCo₂. High temperature cubic phase distorts tetragonally below T_C, then further distorts at T_{SR}, resulting in the orthorhombic structure. A) Temperature dependence of the HoCo₂ lattice parameters. B) Evolution of the normalized c/a ratio. C) Temperature dependence of the unit-cell volume at 0 and 30 kOe applied magnetic field.¹⁸

The basic science of RM₂ compounds is also very intriguing. For example, PrAl₂ shows a tetragonal distortion at T_C, which is fully suppressed by an applied magnetic field as low as 10 kOe, as confirmed by both heat capacity and X-ray powder diffraction data (Figure 5).¹⁹ Interestingly, the nuclear Schottky-specific heat anomaly observed at very low temperatures is unusually high in this compound. DFT calculations point to modification of the energy levels of a nuclear spin system due to the 4f band splitting as a likely reason for the higher Schottky-specific heat close to 0 K in PrAl₂ compared to the elemental Pr. The nuclear-specific heat coefficient, C_N, increases with the increase in the applied magnetic field (Figure 5). The rapid increase of the material's heat capacity below 1 K makes it a promising passive regenerator material for the ultra-low temperature cryo-cooler applications.

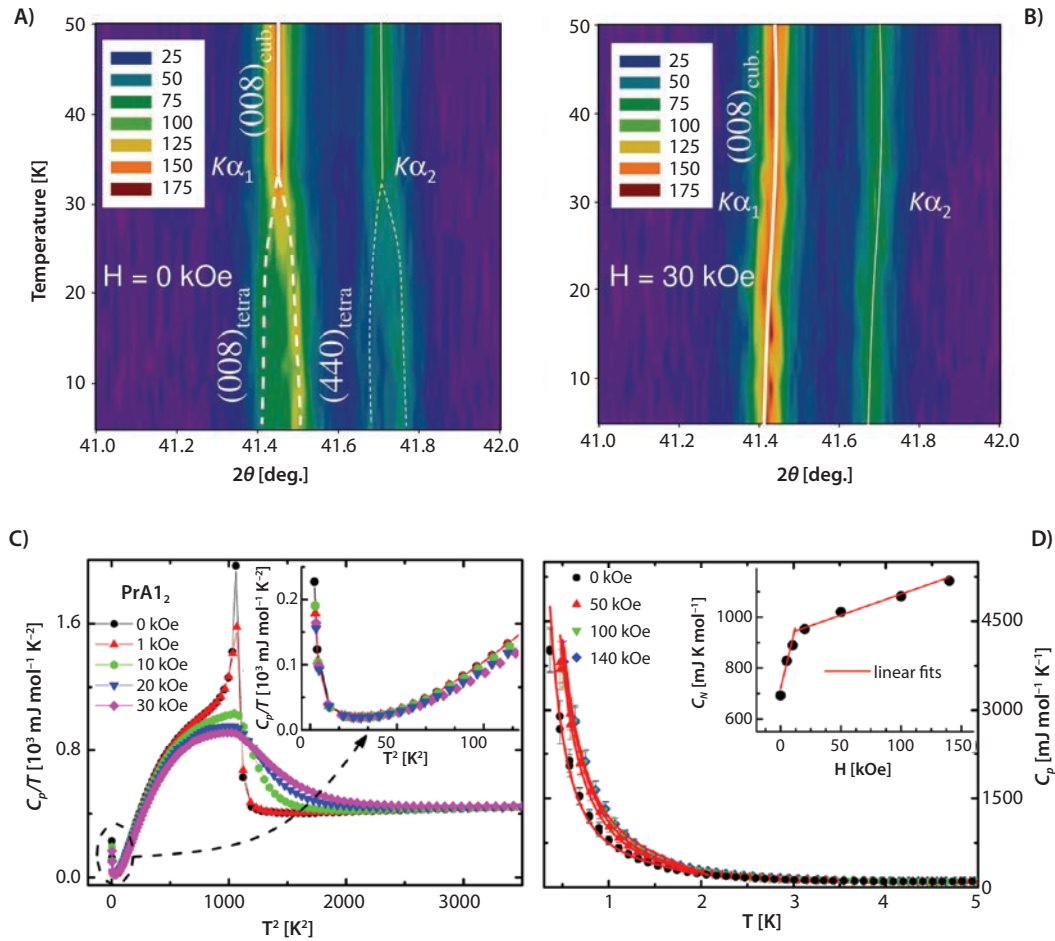


Figure 5. X-ray powder diffraction diagrams of PrAl_2 collected as a function of temperature in A) 0 kOe and B) 30 kOe applied magnetic field. The structural distortion is seen on the zero field data, but it is suppressed in 30 kOe field. C) The heat capacity of PrAl_2 , plotted in C_p/T vs T^2 coordinates highlighting a sharp transition at T_c that becomes smeared above 10 kOe and an upturn below 2 K. D) Schottky nuclear-specific heat anomaly in magnetic fields from 0 to 140 kOe; the inset shows the magnetic field dependence of the nuclear-specific heat coefficient C_n .

Conclusion

Many intermetallic compounds containing lanthanides possess interesting physical behaviors that have great potential for use in energy-related applications. Two interesting and well-studied systems, R_5T_4 and RCo_2 , were highlighted in this review; however, there are undoubtedly many other rare-earth systems both known (e.g., $\text{RFe}_{13-x}\text{Si}_x$) and waiting to be discovered. These anticipated discoveries will push the limits of our basic knowledge and enable the creation of smart multifunctional materials for the technologies of tomorrow.

Acknowledgments

The Ames Laboratory is operated for the U. S. Department of Energy by Iowa State University of Science and Technology under contract No. DE-AC02-07CH11358. The work presented in this review was supported by the Department of Energy, Office of Basic Energy Sciences, Materials Sciences Division.

References

- (1) Mudryk, Y.; Pecharsky, V. K.; Gschneidner, Jr., K. A. R_5T_4 compounds. An extraordinary versatile model system for the solid state science, in: Bunzli, J.-C. and Pecharsky, V. K. Eds., *Handbook on the Physics and Chemistry of Rare Earths*, Elsevier, **2014**, 44, pp. 283-449.
- (2) Gschneidner, Jr., K. A.; Pecharsky, V. K. *Z. Kristallogr.* **2006**, 221, 375.
- (3) Pecharsky, V. K.; Gschneidner, Jr., K. A. *Phys. Rev. Lett.* **1997**, 78, 4494.
- (4) Pecharsky, V. K.; Gschneidner, Jr., K. A. *Appl. Phys. Lett.* **1997**, 70, 3299.
- (5) Levin, E. M. et al. *Phys. Rev. B* **1999**, 60, 7993.
- (6) Morellon, L. et al. *Appl. Phys. Lett.* **1998**, 73, 3462.
- (7) Morellon, L. et al. *Phys. Rev. B* **1998**, 58, R14721.
- (8) Levin, E. M. et al. *Phys. Rev. B* **2001**, 63, 174110.
- (9) Roy, S. B. et al. *Phys. Rev. B* **2006**, 74, 012403.
- (10) Levin, E. M. et al. *Phys. Rev. B* **2004**, 69, 144428.
- (11) Velez, S. et al. *Phys. Rev. B* **2010**, 81, 064437.
- (12) Ouyang, Z. W. et al. *Phys. Rev. B* **2006**, 74, 094404.
- (13) Mudryk, Ya. et al. *Phys. Rev. B* **2008**, 77, 024408.
- (14) Pecharsky, V. K.; Cui, J. I.; Johnson, D. D. *Phil. Trans. R. Soc. A* **2016**, 374, 20150305.
- (15) Yuce, S. et al. *Appl. Phys. Lett.* **2012**, 101, 071906.
- (16) Aleksandryan, V. V. et al. *Sov. Phys. JETP* **1987**, 65, 502.
- (17) Gratz, E. et al. *Phys.: Condens. Matter* **1994**, 6, 6699.
- (18) Mudryk, Y. et al. *J. Mat. Chem. C* **2016**, 4, 4521.
- (19) Pathak, A. K. et al. *Phys. Rev. Lett.* **2013**, 110, 186405.

Metallic Precursors for Magnetic Alloys

For a complete list of available materials, visit aldrich.com/periodic.

Rare Earth Metals

Name	Purity	Resistivity ($\mu\Omega\text{-cm}$)	Form	Prod. No.
Cerium, Ce	99.9% trace rare earth metals basis	73 (20 °C)	chips chunks	461210-50G
	99.9% trace rare earth metals basis	73 (20 °C)	ingot	261041-25G 261041-100G
Dysprosium, Dy	99.9% trace rare earth metals basis	89 (20 °C)	chips	263028-5G
	99.9% trace rare earth metals basis	89 (20 °C)	ingot	261076-10G
Erbium, Er	99.9% trace rare earth metals basis	86 (20 °C)	chips	263052-10G
	99.9% trace rare earth metals basis	86 (20 °C)	foil	693685-1EA
	99.9% trace rare earth metals basis	86 (20 °C)	ingot	261084-10G
Europium, Eu	99.9% trace rare earth metals basis	81 (20 °C)	chips in mineral oil	457965-5G
	99.9% trace rare earth metals basis	81 (20 °C)	ingot	261092-1G
Gadolinium, Gd	99.9% trace rare earth metals basis	126 (20 °C)	chips	263087-10G 263087-50G
	99.9% trace rare earth metals basis	126 (20 °C)	foil	693723-1EA
	99.99% trace rare earth metals basis	126 (20 °C)	ingot	691771-10G
	99.9% trace rare earth metals basis	126 (20 °C)	ingot	261114-10G
	99% trace rare earth metals basis	126 (20 °C)	powder	263060-5G
Lanthanum, La	99.9% trace rare earth metals basis	54	ingot under oil	261130-25G
	99.9% trace rare earth metals basis	54	pieces	263117-25G
Lutetium, Lu	99.9% trace rare earth metals basis	54 (20 °C)	ingot	261149-1G
	99.9% trace rare earth metals basis	54 (20 °C)	foil	693650-1EA
Neodymium, Nd	99.9% trace rare earth metals basis	64.0 (20 °C)	chips	263141-25G
	99.9% trace rare earth metals basis	64.0 (20 °C)	ingot in mineral oil	261157-25G
Praseodymium, Pr	99.9% trace rare earth metals basis	68 (20 °C)	ingot	261173-10G
Samarium, Sm	99.9% trace rare earth metals basis	91.4 (0 °C)	chips	261211-10G
	99.9% trace rare earth metals basis	91.4 (0 °C)	foil	693731-1EA
	99.9% trace rare earth metals basis	91.4 (0 °C)	ingot	263184-10G
	99% trace rare earth metals basis	91.4 (0 °C)	powder or filings	261203-1G 261203-10G 261203-50G
Thulium, Tm	99.9% trace rare earth metals basis	90 (20 °C)	foil	693677-1EA
Ytterbium, Yb	99.9% trace rare earth metals basis	28 (20 °C)	chips	262986-5G
	99.9% trace metals basis	28 (20 °C)	chunks	548804-5G
	99.9% trace rare earth metals basis	28 (20 °C)	foil	693669-1EA
	99.9% trace rare earth metals basis	28 (20 °C)	ingot	261300-5G
Yttrium, Y	99.9% trace rare earth metals basis	57 (20 °C)	chips	262994-5G 262994-25G
	99.8% trace rare earth metals basis	57 (20 °C)	foil	693642-1EA
	99.9% trace rare earth metals basis	57 (20 °C)	ingot	261319-10G 261319-50G

Transition Metals

Name	Purity	Resistivity ($\mu\Omega\text{-cm}$)	Form	Prod. No.
Chromium, Cr	99.995% trace metals basis	12.7 (20 °C)	chips	374849-50G 374849-250G
Cobalt, Co	99.95% trace metals basis	6.24 (20 °C)	foil	356891-5.6G 356891-22.4G 356891-6.25CM2 356891-25CM2
	$\geq 99.99\%$ trace metals basis	6.24 (20 °C)	foil	266671-1.4G
	99.95% trace metals basis	6.24 (20 °C)	foil	356867-2.2G 356867-8.8G
	99.995% trace metals basis	6.24 (20 °C)	granular	203076-5G 203076-25G
	99.95% trace metals basis	6.24 (20 °C)	rod	398810-8.5G 398810-25.5G 398810-150MM 398810-50MM
	99.995% trace metals basis	6.24 (20 °C)	wire	266701-1.4G

Name	Purity	Resistivity ($\mu\Omega\text{-cm}$)	Form	Prod. No.
Iron, Fe	99.98% trace metals basis	9.71	chips	267945-250G 267945-1KG
	$\geq 99.99\%$ trace metals basis	9.71	foil	338141-1.2G 338141-5G 338141-25CM2 338141-6.25CM2
	$\geq 99.9\%$ trace metals basis	9.71	foil	356808-2G 356808-8G 356808-25CM2 356808-100CM2
	$> 99.99\%$ trace metals basis	9.71	granular	413054-5G 413054-25G
	99.98% trace metals basis	9.71	rod	266213-30G 266213-150G
	$\geq 99.99\%$ trace metals basis	9.71	wire	266256-3.1G 266256-15.5G
	$\geq 99.9\%$ trace metals basis	9.71	wire	356824-6.2G 356824-31G 356824-5M 356824-1M
	$\geq 99.9\%$ trace metals basis	9.71	wire	356832-1EA 356832-1.5G
	Manganese, Mn	99%	185 (20 °C)	chips
Nickel, Ni	99.98% trace metals basis	6.97 (20 °C)	foil	357553-2.8G 357553-11.2G 357553-44.8G 357553-100CM2 357553-25CM2 357553-6.25CM2
	99.995% trace metals basis	6.97 (20 °C)	foil	267007-1.4G 267007-5.6G
	99.98% trace metals basis	6.97 (20 °C)	foil	357588-2.2G 357588-8.8G
	$\geq 99.99\%$ trace metals basis	6.97 (20 °C)	rod	267074-14G 267074-42G
	$\geq 99.99\%$ trace metals basis	6.97 (20 °C)	wire	267058-1.7G 267058-8.5G
	Palladium, Pd	99.95% trace metals basis	9.96 (20 °C)	evaporation slug
99.95% trace metals basis		9.96 (20 °C)	evaporation slug	373206-2.4G
99.9% trace metals basis		9.96 (20 °C)	foil	348678-7.6G
99.9% trace metals basis		9.96 (20 °C)	foil	287474-3.8G
99.98% trace metals basis		9.96 (20 °C)	foil	348643-1.9G
99.9% trace metals basis		9.96 (20 °C)	foil	411450-375MG 411450-1.5G
99.9% trace metals basis		9.96 (20 °C)	foil	267120-190MG
99.99% trace metals basis		9.96 (20 °C)	granular	203998-1G 203998-5G
$\geq 99.9\%$ trace metals basis		9.96 (20 °C)	rod	346985-7.6G
99.9% trace metals basis		9.96 (20 °C)	sponge	267082-1G 267082-5G
99.9% trace metals basis		9.96 (20 °C)	wire	267112-900MG 267112-9G
Rhodium, Rh	99.9% trace metals basis	4.33 (20 °C)	foil	357340-190MG
	99.9% trace metals basis	4.33 (20 °C)	wire	277916-1G
Ruthenium, Ru	99.9% trace metals basis	7.1 (0 °C)	sponge	267406-5G

Non-magnetic Metals

Name	Purity	Resistivity ($\mu\Omega\text{-cm}$)	Form	Prod. No.
Aluminum, Al	99.999% trace metals basis	resistivity 2.6548	evaporation slug	433705-25G
	99.7% trace metals basis	resistivity 2.6548	granular	518573-500G
	99.999% trace metals basis	resistivity 2.6548	foil	266957-1EA 266957-27.2G
	99.999% trace metals basis	resistivity 2.6548	foil	266574-3.4G 266574-13.6G 266574-100CM2 266574-25CM2
	99.999% trace metals basis	resistivity 2.6548	foil	326852-100CM2 326852-1.7G 326852-6.8G 326852-25CM2
	$\geq 99.999\%$ trace metals basis	resistivity 2.6548	foil	326860-900MG 326860-3.6G
	$\geq 99.999\%$ trace metals basis	resistivity 2.6548	pellets	326941-25G
	99.99% trace metals basis	resistivity 2.6548	pellets	338788-50G
	99.999% trace metals basis	resistivity 2.6548	rod	202576-10G
	99.999% trace metals basis	resistivity 2.6548	wire	266558-5M 266558-25M 266558-10.5G 266558-52.5G
	$\geq 99.999\%$ trace metals basis	resistivity 2.6548	wire	326887-10M 326887-50M 326887-7G 326887-35G
	99% trace metals basis	resistivity 2.6548	foil	733369-4EA
	99.9995% trace metals basis	resistivity 2.6548	ingot	773964-5EA
	Antimony, Sb	99.999% trace metals basis	resistance 41.7	beads
Bismuth, Bi	99.999% trace metals basis	resistivity 129 (20 °C)	beads	452386-50G
	99.999% trace metals basis	resistivity 129 (20 °C)	pieces	556130-250G
	99.9% trace metals basis	resistivity 129 (20 °C)	shot tear-shaped	265470-500G
Boron, B	99% trace metals basis	resistivity 1.5E12 (20 °C)	crystalline	333360-5G 333360-25G
Gallium, Ga	99.9995% trace metals basis	resistivity 25.795 (30 °C)	-	203319-5G 203319-25G
	99.999% trace metals basis	resistivity 25.795 (30 °C)	-	263273-10G 263273-50G
	99.99% trace metals basis	resistivity 25.795 (30 °C)	-	263265-10G 263265-50G
	99.99999% trace metals basis	resistivity 25.795 (30 °C)	pieces	772631-5G
Germanium, Ge	99.999% trace metals basis	resistivity 53000 (20 °C)	chips	263230-10G 263230-50G
	99.999% trace metals basis	resistivity 53000 (20 °C)	chips	203343-5G 203343-25G
Silicon, Si	99.95% trace metals basis	-	pieces	343250-50G 343250-500G

Magnetocaloric Materials

For a complete list of available materials, visit aldrich.com/magnetic.

Name	Composition	Form	Prod. No.
Dysprosium-Erbium-Aluminum alloy, $Dy_{0.8}Er_{0.2}Al_2$	$Dy_{0.8}Er_{0.2}Al_2$	powder	693499-1G
Gadolinium	Gd	ingot	691771-10G
Gadolinium-silicon-germanium alloy	$Gd_3Ge_2Si_2$	powder and chunks	693510-1G
	$Gd_5Ge_2Si_2$	powder and chunks	693502-1G

MATERIALS FOR INNOVATION



BIOMEDICAL

Materials for drug delivery, tissue engineering, and regenerative medicine; PEGs, biodegradable and natural polymers; functionalized nanoparticles; block copolymers, dendrimers and nanoclays

ELECTRONICS

Nanowires; printed electronics inks and pastes; materials for OPV, OFET, OLED; nanodispersions; CNTs and graphene; precursors for PVD, CVD, and sputtering

ENERGY

Ready-to-use battery grade electrode and electrolyte materials; nanopowders, nanostructures and dispersions; quantum dots; perovskites; fuel cells and membrane; hydrogen storage materials including MOFs; phosphors; thermoelectrics; high purity salts

Find more information on our capabilities at
aldrich.com/matsci

ELEMENTAL BUILDING BLOCKS FOR INNOVATIVE TECHNOLOGY

Goodfellow Alloys and Pure Elements Now Available

High-purity metals and alloys play an essential role in applications such as biomedical engineering and physical vapor deposition. Advances in materials science require materials that ensure optimum properties, performance, and quality. Over **9,900** elemental materials and **7,800** alloys are now available from Goodfellow Cambridge Ltd., a leading international supplier of metals and materials for research and industry.

As materials innovation requires not only the correct composition but also form, our selection of materials includes:

- Foils
- Tubes
- Sheets
- Spheres
- Rods
- Fibers
- Foams
- Powders
- Wires
- Bars
- Honeycombs
- Meshes

Representative Materials

Name	Dimensions	Specifications	Prod. No.
Aluminum-Lithium-Copper Alloy	OD 24 mm; ID 22 mm	99% purity	GF55446295
Carbon, Fiber	0.007 mm diameter	Tex number 200, 3,000 filaments	GF20790558
Iron-Nickel Alloy	45 micron powder	99.9% purity	GF59815435
Tantalum, Tube	OD 0.31 mm; ID 0.19 mm	Trace metal purity, 99.9%	GF33615716
Niobium, Insulated Wire	0.125 mm diameter	Insulated wire, polyimide insulation	GF76912308
Ytterbium, Foil	0.80 mm, 60x60 mm	99% purity	GF14565865

Goodfellow



For a full selection of ultra-high purity materials, visit
go.sigmaldrich.com/itselemental